Spectral–Temporal Simulations of Internal Dissipation Models of Gamma-Ray Bursts

Katsuaki Asano[1], and Peter Mészáros[2]

asano@phys.titech.ac.jp, nnp@astro.psu.edu

ABSTRACT

We present calculations of the time evolution of the prompt spectra of gamma-ray burst models involving generic internal dissipation regions, including internal shocks, either by itself or in the presence of an external photon source such as a photosphere. The method uses a newly developed time-dependent code involving synchrotron emission and absorption, inverse Compton scattering and pair formation. The models reproduce the typically observed Band spectra and their generic time evolution, including the appearance of an extra keV-GeV component, whose delay in simple SSC models, however, is only partially able to explain the several seconds observed GeV delays. On the other hand, models involving both a photosphere and an internal dissipation region at a larger radius produce both an extra GeV component and time delays which are in the range of the observations.

Subject headings: gamma rays burst: general — Radiation mechanisms: non-thermal

1. Introduction

Most of the prompt emission spectra of gamma-ray bursts (GRBs) can be described by the well-known Band function (Band et al. 1993), which has a spectral peak around the MeV range. Since the EGRET era (González et al. 2003), distinct spectral components

---

[1]Interactive Research Center of Science, Tokyo Institute of Technology, 2-12-1 Ookayama, Meguro-ku, Tokyo 152-8550, Japan

[2]Department of Astronomy & Astrophysics; Department of Physics; Center for Particle Astrophysics; Pennsylvania State University, University Park, PA 16802

in higher energy ranges have been reported. Moreover, bright optical emissions during the prompt phase, such as in GRB 080319B (Racusin et al. 2008), have also been detected. Such lower energy emissions also consist of distinct spectral components. In the popular internal shock model of GRB the prompt MeV gamma-rays are attributed to synchrotron radiation from electrons accelerated in shocks within the GRB outflow (Piran 2005; Mészáros 2006), while higher energy photons are attributed to inverse Compton (IC) upscattering of these synchrotron photons, a scheme called synchrotron self-Compton or SSC (Mészáros & Rees 1994; Pilla & Loeb 1998; Panaitescu & Mészáros 2000; Guetta & Granot 2003). Variants on this scheme involve having the MeV photons, whether of synchrotron or other origin, arising at a different location (usually at a smaller radius) than the location where they are upscattered, a scheme refereed to as external inverse Compton or EIC (Beloborodov 2005; Toma et al. 2009; Murase et al. 2011). The generic radiation physics is independent, to a large degree, of the specific macroscopic model for the acceleration of the radiating or scattering non-thermal particles. Thus, the results we discuss here are not tied specifically to internal shock models, but apply also to more generic dissipative models, in which synchrotron, IC and, in the case of high radiation density also pair formation, are the main radiation mechanisms.

The recent observations over a wide range of photon energies by the *Fermi*-Large Area Telescope (LAT) and GLAST Burst Monitor (GBM) instruments and robotic optical telescopes such as TORTORA have stimulated research on the temporal evolution of the GRB spectra, which is a key for distinguishing various models. Several authors have developed time-dependent codes and discuss the spectral evolution in GRBs (Pe'er & Waxman 2005; Pe'er 2008; Belmont et al. 2008; Vurm & Poutanen 2009; Bošnjak et al. 2009; Daigne et al. 2011). Some of those studies focus on the effects of the dynamical evolution of the shocked region, multiple Compton scattering, or thermal particles etc. An expanding range of physical situations needs to be considered, in view of the ongoing observational and theoretical progress being made. Here, we improve our previous Monte Carlo code, developed in a series of studies for hadronic and leptonic processes (see, e.g., Asano & Inoue 2007), into a time-dependent code. Our code is based on the one-zone approximation with the Lagrangian specification in the energy space for particles. Although we plan to develop this code to deal with the hadronic processes in the future, at this time only the leptonic processes are included, as a first step.

Our goal in this paper is to study the temporal behavior of the radiation field in the typical types of geometries generally considered in GRB models. In particular, we study the development of the photon spectra as a function of time, as well as the expected light curves in specific energy ranges, in order to gain insight into current questions such as the origin of the delay between MeV and GeV pulses in bursts observed by the *Fermi* (Abdo et al.

2009c,b; Ackermann et al. 2011), or the presence of additional spectral components above or below (Abdo et al. 2009a,b; Ackermann et al. 2011) the usual Band (MeV) spectra known from previous Compton and *Swift* studies.

In §2 we present the basic physical model used in our numerical, discussing the various physical processes involved and the way the time-dependent spectra and light curves are computed. The results are presented in §3. In subsection §3.1 we discuss first three cases characterized by parameters such as inferred from pre-Fermi GRB observations, in the context of an SSC model. These "moderate" models serve as a reference point, providing insight into what was missed in the pre-Fermi observations. In subsection §3.2 we explore the temporal and spectral properties and predictions for bursts with parameters which might characterize some of the more interesting bursts observed by the Fermi LAT instrument, again based on an SSC model. In §3.3 we discuss the properties of a model including external photon sources providing a Band function spectrum which is reprocessed and upscattered at a different location. We summarize our numerical results in §4 and discuss their relevance and implications in §5.

2. Model and Methods

In order to simulate the temporal evolution of photon emissions, we develop a new numerical code by improving our code matured via a series of GRB studies (Asano 2005; Asano & Nagataki 2006; Asano & Inoue 2007; Asano et al. 2009b), in which the photon spectrum had been obtained with the steady-state approximation for the photon field.

Here we consider a shell expanding with the Lorentz factor Γ from an initial radius $R = R_0$. The calculation of the photon production is carried out in the shell frame (hereafter, the quantities in this frame are denoted with primed characters). This shell represents the internal dissipation region, which in what follows will be referred to as "internal shock", although it could be a generic dissipation region resulting in particle acceleration, e.g., a magnetic reconnection zone, etc. Let us adopt notations for particle kinetic energies of electrons and photons as $\varepsilon_{\mathrm{e}} = (\gamma_{\mathrm{e}} - 1)m_{\mathrm{e}}c^2$ and ε_{γ}, respectively. The one-zone approximation with a constant shell width $W' = R_0/\Gamma$ is adopted so that the photon density $n'_{\gamma}(\varepsilon'_{\gamma})$ and magnetic field B', etc., in the shell are homogeneous. We refresh the photon field with a time step $\Delta T' = R/(100\Gamma c)$, during which electrons/positrons emit photons in the constant photon field. With the same time step we inject electrons intermittently. In this paper, we assume a constant injection rate with total energy $E_{\mathrm{e}} = \Gamma E'_{\mathrm{e}}$ during a timescale $t'_{\mathrm{inj}} = W'/c$. The injection spectrum is assumed as a cut-off power-law shape, $\dot{N}'_{\mathrm{e,inj}}(\varepsilon'_{\mathrm{e}}) \propto \varepsilon'^{-p}_{\mathrm{e}} \exp\left(-\varepsilon'_{\mathrm{e}}/\varepsilon'_{\mathrm{max}}\right)$ for $\varepsilon'_{\mathrm{e}} > \varepsilon'_{\mathrm{min}}$, where $\varepsilon'_{\mathrm{max}}$ is determined by equating the

cooling timescale $t'_{\rm cool}$ and the acceleration timescale $t'_{\rm acc} = \xi \varepsilon'_{\rm e}/ceB'$ (hereafter, the efficient acceleration of $\xi = 1$ is supposed). Using the cooling rates due to synchrotron ($\dot{\mathcal{E}}_B$) and IC ($\dot{\mathcal{E}}_{\rm IC}$), and the heating rate due to synchrotron self absorption (SSA) ($\dot{\mathcal{E}}_{\rm SA}$), the cooling time is defined as $t_{\rm cool} = \varepsilon_{\rm e}/(\dot{\mathcal{E}}_B + \dot{\mathcal{E}}_{\rm IC} - \dot{\mathcal{E}}_{\rm SA})$.

The cooling timescale would be much shorter than the time step $\Delta T'$. An even shorter time step $\Delta t' = \min(\Delta T'/10, t'_{\rm cool}/100)$ is used to evolve the electron energy distribution during $\Delta T'$ by following each electron with the Lagrangian specification in the energy space. In every time step $\Delta t'$, we accumulate emitted photons, and add them to the photon field $n'_\gamma(\varepsilon'_\gamma)$ in every $\Delta T'$. In the following subsection we explain the detailed methods to estimate $t'_{\rm cool}$ and simulate the emission processes. The methods are essentially the same as our old code.

2.1. Physical processes

2.1.1. Synchrotron emission

The energy loss rate due to synchrotron/cyclotron emission is

$$\dot{\mathcal{E}}_B = \frac{1}{4\pi}\sigma_{\rm T}cB^2\gamma_{\rm e}^2\beta_{\rm e}^2\sin^2\alpha, \tag{1}$$

where $\sigma_{\rm T}$ is the Thomson cross section, and α is the pitch angle (Rybicki & Lightman 1979). In the ultra-relativistic limit ($\gamma_{\rm e} \gg 1$), the energy spectrum of synchrotron emission per unit time per photon energy is written as

$$P_B(\varepsilon_{\rm e}, \varepsilon_\gamma) = \frac{\sqrt{3}e^3 B\sin\alpha}{2\pi\hbar m_{\rm e}c^2}F(x), \tag{2}$$

$$x \equiv \frac{2m_{\rm e}c\varepsilon_\gamma}{3\gamma_{\rm e}^2\hbar eB\sin\alpha}, \tag{3}$$

where $F(x)$ is the synchrotron function. In the non-relativistic energy range, instead of the exact formula (see, e.g., Pe'er & Waxman 2005), we adopt a simple approximation (Ghisellini et al. 1998) for $\beta_{\rm e} = \sqrt{1 - 1/\gamma_{\rm e}^2} < 0.89$ as

$$P_B(\varepsilon_{\rm e}, \varepsilon_\gamma) = \frac{m_{\rm e}c^2\sigma_{\rm T}B}{3\pi\hbar e}\frac{\gamma_{\rm e}^2\beta_{\rm e}^2}{1 + 3\gamma_{\rm e}^2\beta_{\rm e}^2}\exp\left[\frac{2(1 - \varepsilon_\gamma/\varepsilon_B)}{1 + 3\gamma_{\rm e}^2\beta_{\rm e}^2}\right], \tag{4}$$

$$\varepsilon_B \equiv \frac{\hbar eB}{m_{\rm e}c}, \tag{5}$$

for the isotropic distribution of electrons.

2.1.2. Inverse Compton

In order to calculate emission due to photon scattering with electrons, we prepared tables in advance. Since we plan to develop this code to simulate optically thick plasmas in the future, the tables cover a wide energy range from the Thomson regime to the Klein-Nishina limit. In the laboratory frame, the photon distribution is assumed to be isotropic. Integrating over incident and scattering angles with the Monte Carlo method, we obtained the tables of the emission spectrum as below. Here, we denote the quantities in the electron rest frame by characters with tilde. Given the energies of an electron ε_e and an incident photon $\varepsilon_{\gamma,in}$ and a cosine of incident angle μ_{in}, the Lorentz transformation yields the photon energy in the electron rest frame $\tilde{\varepsilon}_{\gamma,in}$. The energy of the scattered photon depends on the cosine of the scattering angle $\tilde{\mu}$ as

$$\tilde{\varepsilon}_{\gamma,out} = \frac{\tilde{\varepsilon}_{\gamma,in}}{1 + (\tilde{\varepsilon}_{\gamma,in}/m_e c^2)(1 - \tilde{\mu})}. \tag{6}$$

The scattering probability against $\tilde{\mu}$ is

$$\mathcal{P}_{\tilde{\mu}} \propto \left(\frac{\tilde{\varepsilon}_{\gamma,out}}{\tilde{\varepsilon}_{\gamma,in}}\right)^2 \left[\frac{\tilde{\varepsilon}_{\gamma,in}}{\tilde{\varepsilon}_{\gamma,out}} + \frac{\tilde{\varepsilon}_{\gamma,out}}{\tilde{\varepsilon}_{\gamma,in}} - (1 - \tilde{\mu}^2)\right], \tag{7}$$

which should be normalized by the total cross section as

$$\begin{aligned}
\sigma_{KN} &= \frac{3}{4}\sigma_T \left[\frac{1+x}{x^3}\left(\frac{2x(1+x)}{1+2x} - \ln(1+2x)\right) + \right. \\
&\quad \left. \frac{\ln(1+2x)}{2x} - \frac{1+3x}{(1+2x)^2}\right], \tag{8} \\
x &\equiv \tilde{\varepsilon}_\gamma/m_e c^2, \tag{9}
\end{aligned}$$

(Rybicki & Lightman 1979). Reverting to the laboratory frame again, we obtain the tables of the emission spectrum normalized by the photon density in a form of

$$P_{IC}(\varepsilon_e, \varepsilon_{\gamma,in}, \varepsilon_{\gamma,out})/n_\gamma(\varepsilon_{\gamma,in}). \tag{10}$$

At the same time we obtain the tables of the "photon-absorption" probability for incident photons, which assures the conservation of the photon number in the scattering process. The Monte Carlo integral over the angles brings us another table of the average value,

$$\overline{\Delta\varepsilon_\gamma\sigma_{KN}} \equiv \overline{(1 - \beta_e\mu_{in})(\varepsilon_{\gamma,out} - \varepsilon_{\gamma,in})\sigma_{KN}}, \tag{11}$$

which is useful to calculate the energy loss rate as

$$\begin{aligned}
\dot{\mathcal{E}}_{IC} &= c\int d\varepsilon_\gamma n_\gamma(\varepsilon_\gamma)\overline{\Delta\varepsilon_\gamma\sigma_{KN}(\varepsilon_e, \varepsilon_\gamma)} \\
&= \int d\varepsilon_\gamma d\varepsilon_{\gamma,out} P_{IC}(\varepsilon_e, \varepsilon_\gamma, \varepsilon_{\gamma,out}). \tag{12}
\end{aligned}$$

2.1.3. Synchrotron self-absorption

Adopting the synchrotron/cyclotron formulae in §2.1.1, the cross section of SSA (Rybicki & Lightman 1979; Ghisellini & Svensson 1991) is written as

$$\sigma_{\mathrm{SA}} = \frac{c^2 h^3}{8\pi\varepsilon_\gamma^3}\left(\frac{\gamma_{\mathrm{abs}}^2 \beta_{\mathrm{abs}}}{\gamma_{\mathrm{e}}^2 \beta_{\mathrm{e}}}P_B(\varepsilon_{\mathrm{abs}},\varepsilon_\gamma) - P_B(\varepsilon_{\mathrm{e}},\varepsilon_\gamma)\right), \tag{13}$$

$$\varepsilon_{\mathrm{abs}} = (\gamma_{\mathrm{abs}}-1)m_{\mathrm{e}}c^2 = \varepsilon_{\mathrm{e}} + \varepsilon_\gamma, \tag{14}$$

A fraction $1 - \exp\left(-c\Delta t' \int d\varepsilon_{\mathrm{e}} n_{\mathrm{e}}\sigma_{\mathrm{SA}}\right)$ of photons will be absorbed every time step. The accumulated amount of absorbed photons is counted in every $\Delta T'$. The heating rate of electrons due to SSA is

$$\dot{\mathcal{E}}_{\mathrm{SA}} = \int d\varepsilon_\gamma c\varepsilon_\gamma \sigma_{\mathrm{SA}} n_\gamma(\varepsilon_\gamma). \tag{15}$$

2.1.4. Electron-Positron pair creation

In order to take into account $\gamma\gamma$-pair creation, every time step $\Delta T'$ we eliminate a fraction of photons, $1 - \exp\left(-\tau_\pm\right)$, with

$$\tau_\pm(\varepsilon_{\gamma,1}) = c\Delta T' \int d\varepsilon_{\mathrm{e}} d\Omega_{\mathrm{in}} (1-\mu_{\mathrm{in}})\frac{n_\gamma(\varepsilon_{\gamma,2})}{4\pi}\sigma_\pm, \tag{16}$$

where

$$\sigma_\pm = \frac{3}{16}\sigma_{\mathrm{T}}(1-y^2)\left[(3-y^4)\ln\frac{1+y}{1-y} - 2y(2-y^2)\right], \tag{17}$$

$$y^2 \equiv 1 - (2m_{\mathrm{e}}^2 c^4)/[\varepsilon_{\gamma,1}\varepsilon_{\gamma,2}(1-\mu_{\mathrm{in}})] \tag{18}$$

(Berestetskii et al. 1982). The integral over the photon energy and incident solid angle $d\Omega_{\mathrm{in}} = 2\pi d\mu_{\mathrm{in}}$ is numerically calculated with the isotropic photon distribution. We simultaneously inject secondary electron/positron pairs. To save computational cost, we adopt a simple approximation for the energy of the secondary pairs as $\varepsilon_{\mathrm{e}} = (\varepsilon_{\gamma,1}+\varepsilon_{\gamma,2})/2 - m_{\mathrm{e}}c^2$ and neglect the effect of electron-positron pair annihilation.

2.1.5. Shell expansion

We take into account the effect of adiabatic cooling, though it may be a minor effect in GRB physics. The adiabatic cooling of the collisionless plasma is not trivial. The motion

of electrons/positrons is controlled by only magnetic fields. If a homogeneous magnetic field evolves according to volume expansion, only the momentum component perpendicular to the magnetic field would be affected. However, the magnetic field in the GRB sources may be highly entangled so that the pitch angle diffusion cannot be neglected. Thus, in this paper, we use a simple isotropic approximation for the "momentum", $\sqrt{\varepsilon_e'^2 + 2m_e c^2 \varepsilon_e'}\, c^{-1} \propto V'^{-1/3}$, which is applicable from non-relativistic ($\varepsilon_e' \propto V'^{-2/3}$) to ultra-relativistic ($\varepsilon_e' \propto V'^{-1/3}$) limits. The constant shell width W' assumed in this paper implies that the volume evolves as $V' = 4\pi R^2 W' \propto R^2$. The volume expansion may imply evolution of the magnetic field, but we assume constant B' for simplicity in this paper.

2.1.6. Photon escape

The photon density n_γ' refreshed every time step gives us the photon escape rate per unit surface as $n_\gamma' c/4$. The photons escape from both the foreside and backside surfaces of the shell (the total surface: $2 \times 4\pi R^2$). Every time step we extract a fraction of photons, $2\pi R^2 c \Delta T'/V' = c\Delta T'/(2W')$.

2.2. Light Curve

We consider photons escaping from the shell with latitudes $\theta \leq \theta_{\rm jet}$ to take into account the jetted structure, but the maximum latitude is taken as large as $\theta_{\rm jet} \equiv 5/\Gamma$ so that the effect of collimation does not affect observation very much. The energy and escape time t' of photons coming from a latitude θ are transformed into energy- and time-bins in observer's frame with

$$\varepsilon_{\rm obs} = \frac{\varepsilon_\gamma'}{\Gamma(1 - \beta_{\rm sh}\cos\theta)(1+z)}, \tag{19}$$

and

$$t_{\rm obs} = (1+z)\left[(1 - \beta_{\rm sh}\cos\theta)\Gamma t' + R_0(1 - \cos\theta)/c\right], \tag{20}$$

respectively, where $\beta_{\rm sh} \equiv \sqrt{1 - 1/\Gamma^2}$. Every time step $\Delta T'$ the spectral number of escaped photons per unit solid angle and surface is estimated with the photon density n_γ' as

$$\frac{dN'(\varepsilon_\gamma')}{d\Omega' dS'} = |\cos\theta'|\frac{n_\gamma'(\varepsilon_\gamma')}{4\pi}c\Delta T', \tag{21}$$

where we count photons escaped from both foreside ($\cos\theta' \geq 0$) and backside ($\cos\theta' \leq 0$) of the shell with the Lorentz transformation for θ

$$\cos\theta' = \frac{\cos\theta - \beta_{\mathrm{sh}}}{1 - \beta_{\mathrm{sh}}\cos\theta}. \tag{22}$$

For high latitude emissions with $\cos\theta' \leq 0$, the shell thickness adds an extra "time delay"

$$\Delta t_{\mathrm{bk}} = (1+z)\frac{W'\Gamma}{c}\left(\cos\theta - \beta_{\mathrm{sh}}\right), \tag{23}$$

in Eq. (20). The number of photons escaping from a surface element $\Delta S'$

$$\frac{dN'(\varepsilon'_\gamma)}{d\Omega'dS'}\Delta S', \tag{24}$$

is transformed to the frame of the central engine with

$$dS' = dS = 2\pi R^2\sin\theta d\theta,\, d\Omega' = \frac{d\Omega}{\Gamma^2(1 - \beta_{\mathrm{sh}}\cos\theta)^2},\, dN' = dN. \tag{25}$$

In each corresponding time-bin, the observer counts the contribution from ΔS for the photon number per unit surface as

$$\frac{dN_{\mathrm{obs}}}{dS_{\mathrm{obs}}} = \frac{1}{D_{\mathrm{p}}^2}\frac{dN}{d\Omega dS}\Delta S, \tag{26}$$

where the proper distance $D_{\mathrm{p}} = D_{\mathrm{L}}/(1+z)$ is used, because we have already included the effects of the energy shift and time-dilation due to cosmological redshift in eqs. (19) and (20). Integrating over the surface with $0 \leq \theta \leq \theta_{\mathrm{jet}}$, we obtain the total fluence for each time-bin.

As was calculated in Murase et al. (2007), the photon absorption due to extra galactic background light (EBL) is estimated by accumulating the optical depth between the source and observer with the EBL model of Kneiske et al. (2004) (best-fit).

3. Results

The model parameters are five: the initial radius R_0, the bulk Lorentz factor Γ, the comoving magnetic field B', the electron injection energy E_{e}, and the minimum electron energy $\varepsilon'_{\mathrm{min}}$. While we can consider more complicated situations by evolving e.g., B', W', Γ, the electron injection rate, etc., with R, we adopt here for simplicity the constant values of the parameters as mentioned in §2. The other fixed parameters are the jet opening angle

$\theta_{\rm jet} = 5/\Gamma$, electron injection index $p = 2.5$, and the parameter for the electron acceleration timescale $\xi = 1$.

Since we make no assumption about the energy density of the "thermal" components, the conventional parameters of the energy fraction to the total internal energy density, such as $\epsilon_{\rm e}$ and ϵ_B (see the definitions in Mészáros 2006), are not specified. But assuming $\epsilon_{\rm e} = 0.5$ with the electron energy density $E_{\rm e}/(4\pi R_0^3)$, hereafter we will take ϵ_B as a referential value for each parameter set. The Thomson optical depth is another criterial parameter. The electron number density in our simulations can be approximated as

$$n'_{\rm e} = \frac{(p-2)E_{\rm e}}{(p-1)4\pi\varepsilon'_{\rm min}R_0^3}. \tag{27}$$

In all our simulations, the Thomson optical depth $\tau_{\rm T} = n'_{\rm e}\sigma_{\rm T}R_0/\Gamma$ is much smaller than unity.

3.1. GRBs with "Moderate" Parameters

In this subsection we discuss three cases labeled Run1, Run2, and Run3, whose parameters are indicated in the following figures 1-8. In Figure 1, we show the evolution of the spectral photon density in the shell frame for Run1. The model parameter set is one to be considered as fiducial values before the *Fermi* satellite was launched (if $\epsilon_{\rm e} = 0.5$, $\epsilon_B = 0.0025$; $\tau_{\rm T} = 0.03$). As the electron injection proceeds from $R/R_0 = 1$, the photon energy density gradually grows. In this case the energy density of the magnetic field is $\sim 4 \times 10^6$ erg cm^{-3}, which can be compared with the vertical axis in Figure 1. At an early stage (see $R/R_0 = 1.1$ in Figure 1) synchrotron emission is the dominant cooling process for injected electrons so that the spectral peak associated with $\varepsilon'_{\rm min}$ is seen at a few keV. The relatively low photon density at this time leads to a higher cut-off energy (~ 10 MeV) due to $\gamma\gamma$-absorption. As the photon energy density increases, the IC component gradually becomes prominent (see $R/R_0 = 1.2$ and 1.5), and the cut-off energy due to $\gamma\gamma$-absorption decreases. This late growth of the IC component has been observed also in the simulations of Bošnjak et al. (2009). The IC component makes the spectrum so hard that the synchrotron peak gradually disappears, and instead, $\gamma\gamma$-absorption produces a spectral peak at a few hundreds keV.

Below the synchrotron peak energy at a few keV, the synchrotron photons from cooled electrons of $\varepsilon'_{\rm e} < \varepsilon'_{\rm min}$ make a power-law spectrum with the photon index ~ -1.5. The low-energy cut-off due to SSA is clearly seen at ~ 0.1 eV. The electron heating via SSA (Ghisellini et al. 1988) makes a spectral bump just above the cut-off energy. At the end of the electron injection ($R/R_0 = 2$), the superposition of the synchrotron and IC components

shows a hard power-law spectrum above the synchrotron peak energy. Considering the Klein-Nishina effect, the majority of seed photons for the IC process would be low-energy photons at ~ 1 eV. Above the cut-off energy at a few hundreds keV, photon production and $\gamma\gamma$-absorption balance with each other, and consequently generate a steep power-law spectrum. After the electron injection stops, the shell expansion and photon escape dilute the photon density (see the line of $R/R_0 = 2.5$). In this stage, the photon production is practically terminated so that our calculation based on the one-zone approximation shows a sharp cut-off above the $\gamma\gamma$ cut-off energy. The photon energy density in the shell frame at $R/R_0 = 2$ is 1.4×10^8 erg cm^{-3}, which is close to the simple estimate (note that W' is constant) $E_e/(4\pi R^2 R_0)$ with $R = 2R_0$, 2.0×10^8 erg cm^{-3}.
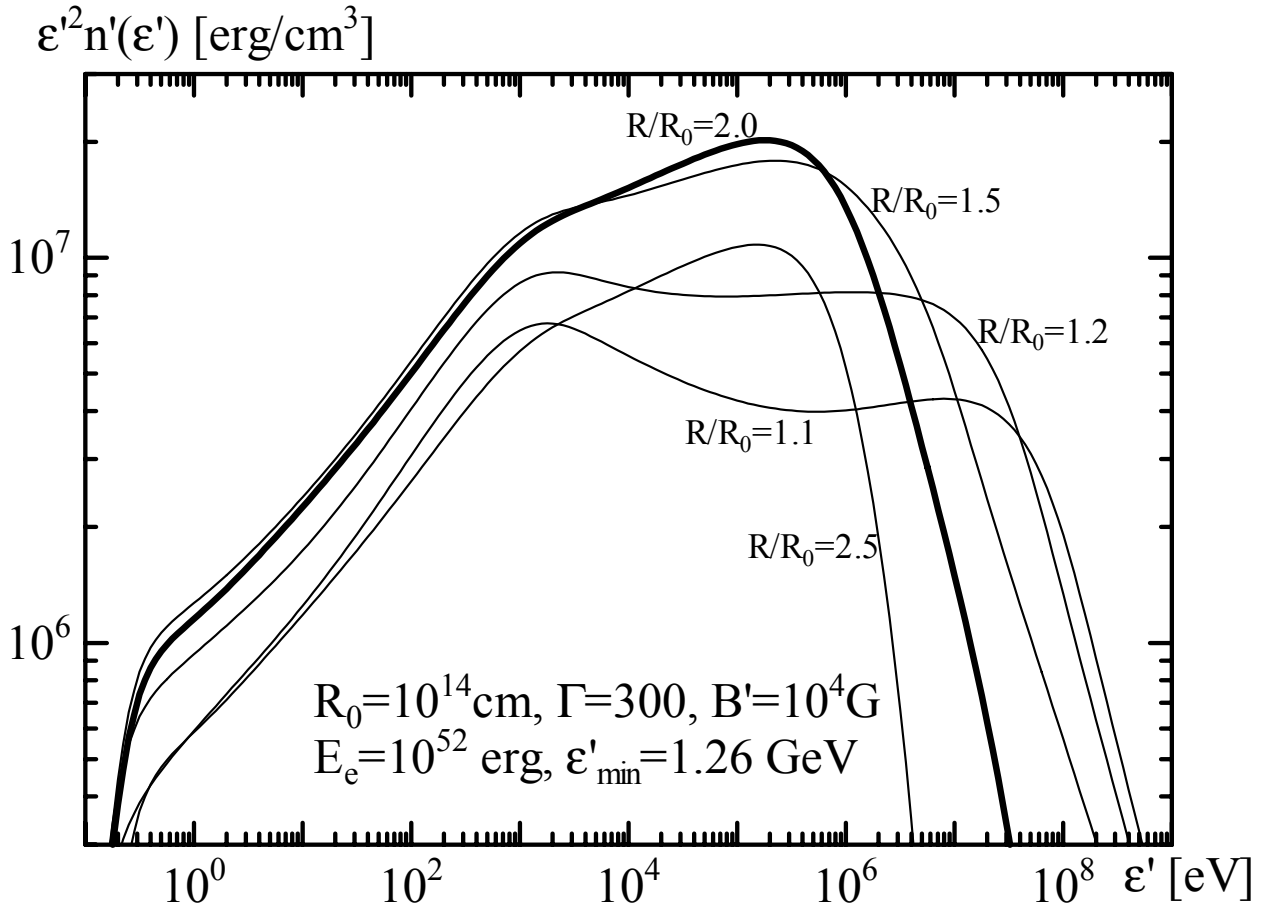
Fig. 1.— Temporal evolution of spectral energy density of photons in the shell frame for Run1. The model parameters are denoted inside the figure. The electron injection is ended at $R/R_0 = 2.0$ (thick line).

According to the method described in §2.2, we plot light curves based on the spectral
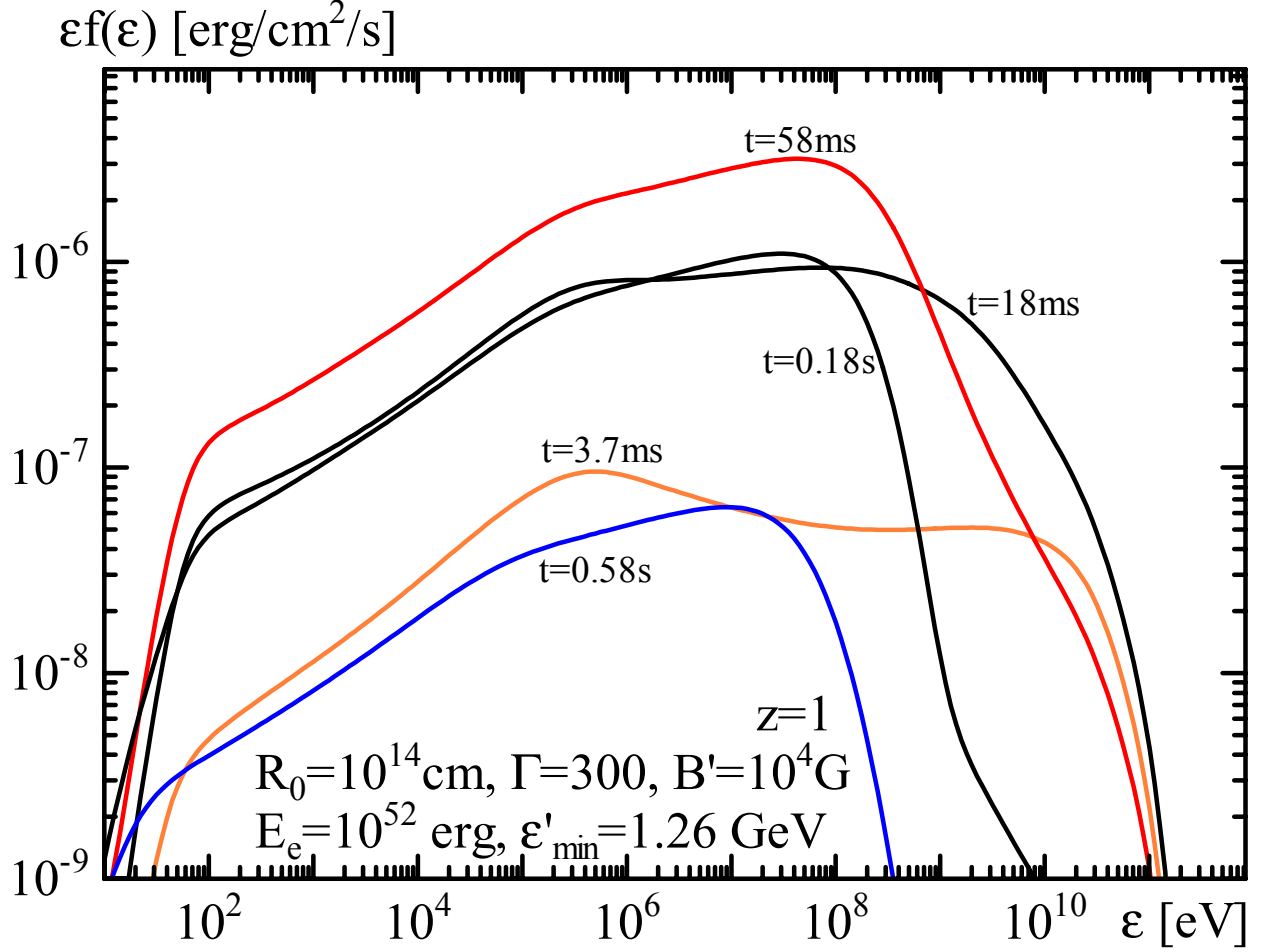
Fig. 2.— Temporal evolution of the observable spectral photon flux for the model described in Figure 1 (Run1). The time-bins are the same as in Figure 3, and the denoted times are the center for each time-bin.

flux (the unit is erg cm^{-2} s^{-1} eV^{-1}) assuming the source redshift of $z = 1$ in Figure 3. The time-bins are logarithmically divided (0.25 dex normalized by $(1 + z)R_0\Gamma^{-2}c^{-1}$), and the flux is averaged over each time-bin. In the figure, the GeV, 100 MeV, and 100 keV light curves are plotted. The keV light curve practically overlaps with the 100 keV lightcurve, and the light curve shapes seem to reproduce well the typical FRED (fast rise, exponential decay; Fenimore et al. 1996) shape, which is frequently found in many GRBs. Reflecting the temporal decrease of the $\gamma\gamma$ cut-off energy in the source, the GeV flux peaks earlier than the lower energy fluxes. This corresponds to what one would get from an extrapolation of the "positive spectral lags", observed in many of the pre-Fermi bursts (Norris et al. 1996) (see also §3.2), to the GeV energy range. This behavior is explicitly interpreted by the evolution

of the photon spectrum shown in Figure 2. Before the peak time of the 1 keV-100 MeV fluxes ($\sim$ 58 ms), the spectrum seems to reflect the evolution of the spectrum in the source frame. During the decaying phase, the spectrum gradually shifts to lower energy owing to the emissions from higher latitudes of the shell (curvature effect). We can see that GeV emission ceases faster than lower energy bands, which explains the narrow pulse shape in the GeV light curve. As shown in Figure 4, however, the GeV fluence is dim compared to the MeV-fluence in this parameter set.
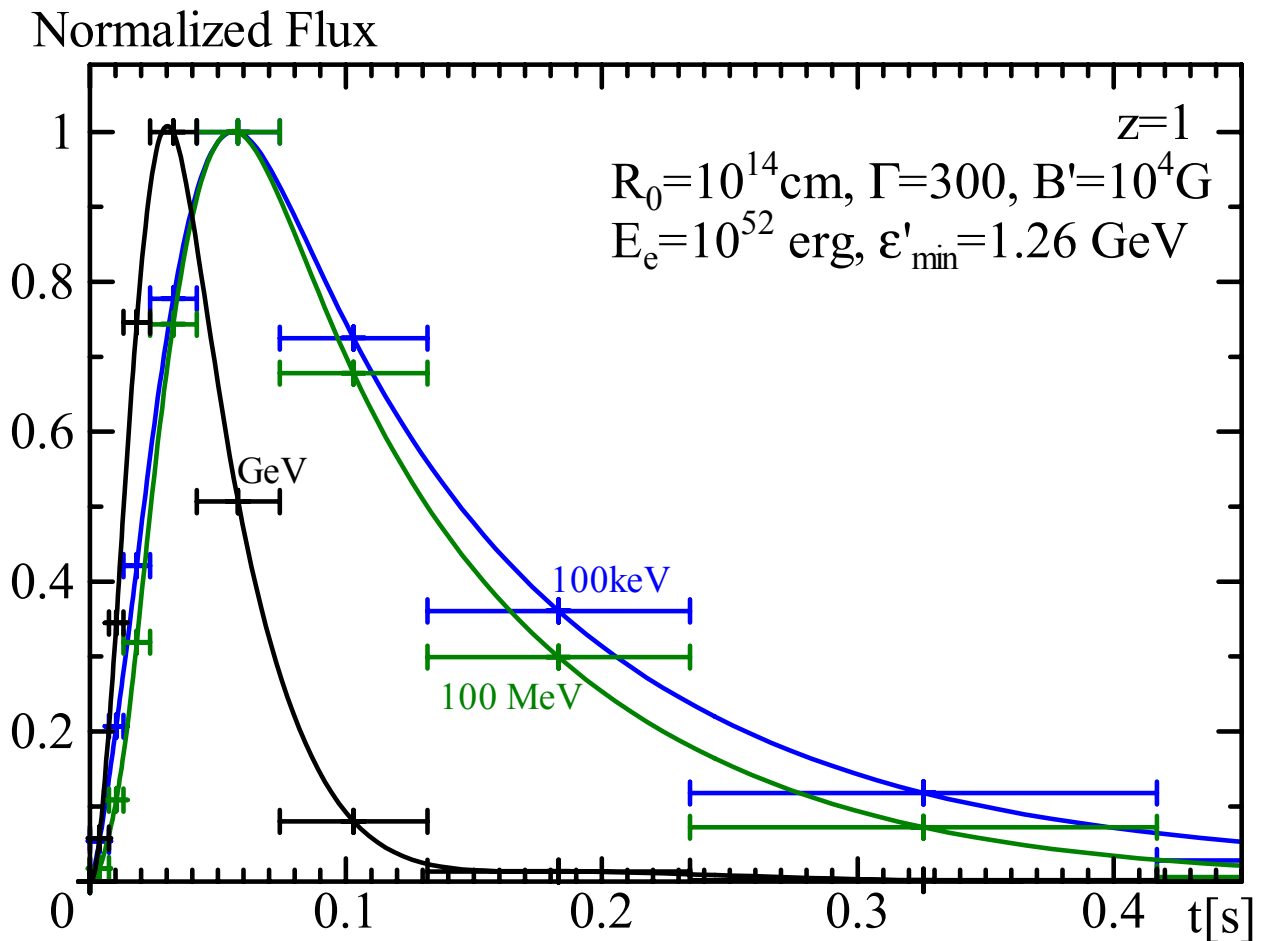
Fig. 3.— Light curves for the model described in Figure 1 (Run1). The plotted values are normalized by the maximum flux. We smoothly join the fluxes averaged over respective time-bins with solid curves for reference.

We have shown the results for Run1 as an example that shows a remarkably suggestive evolution of the spectral shape. However, the high-energy spectral index is harder than the typical observed ones. Hence, we consider two different cases, in which the internal $\gamma\gamma$-absorption for GeV photons is not efficient, and the IC component is not so prominent; Run2
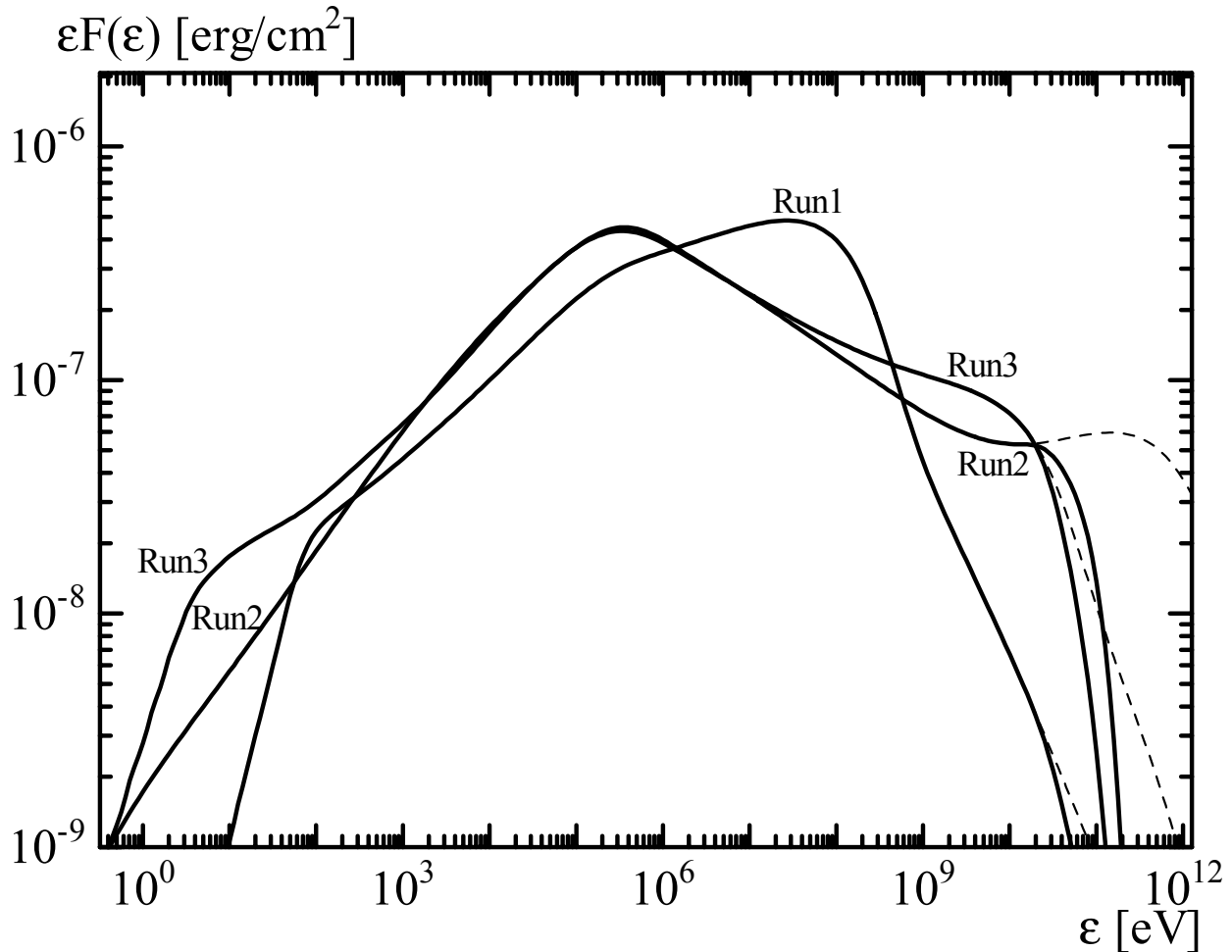
Fig. 4.— Summarized observable fluences for Run1-Run3 with $z = 1$. The dashed lines denote the cases neglecting $\gamma\gamma$-absorption due to EBL.

with large Γ and R_0 (Figures 5 and 6; if $\epsilon_e = 0.5$, $\epsilon_B = 0.06$; $\tau_T = 3 \times 10^{-6}$), and Run3 with moderate Γ and large magnetic field (Figures 7 and 8; if $\epsilon_e = 0.5$, $\epsilon_B = 0.025$; $\tau_T = 9 \times 10^{-5}$). The relatively stronger magnetic field than that in Run1 and the Klein-Nishina effect make synchrotron radiation the dominant cooling process even though $\epsilon_e > \epsilon_B$. In these cases the evolution of the fluxes (Figures 5 and 7) are monotonic compared to Run1.

In Figure 5 the low-energy spectrum below $\varepsilon_{\rm peak} \simeq 300\text{-}400$ keV becomes soft with time. The slow electron cooling due to the low magnetic field in Run2 causes the slow evolution of the low-energy spectrum. The typical energy of electrons emitting 1 eV synchrotron photons is ~ 8 MeV. The synchrotron cooling time for such electrons ~ 550 s is slightly longer than $t'_{\rm inj} \sim 100$ s, although the IC cooling is marginally important even after $t' = t'_{\rm inj}$. This is the

reason for the slow spectral evolution, but note that $t'_{\rm cool}$ for electrons of $\varepsilon'_{\rm min}$ is much shorter than the dynamical timescale. So almost all the energy injected in the shell is released as photons even in this case. For Run2 the SSA frequency is well below the optical band so that we can expect bright optical pulses as shown in Figure 4. While the light curves for keV-100 GeV regions are almost the same as the 100 keV light curve in Figure 6, the optical (~ 1 eV) light curve shows a significant delay relative to the higher energy bands. This delay is a direct consequence of the gradual softening of the low-energy spectrum. The broader pulse profile of the 1 eV light curve compared to that of the 100 keV light curve seen in Figure 6 is due to the emission from higher latitudes. As shown in Figure 4, the intrinsic spectrum for Run2 extends as far as the 1 TeV range, where the IC component dominates, but such photons are absorbed by EBL in our assumption of $z = 1$.
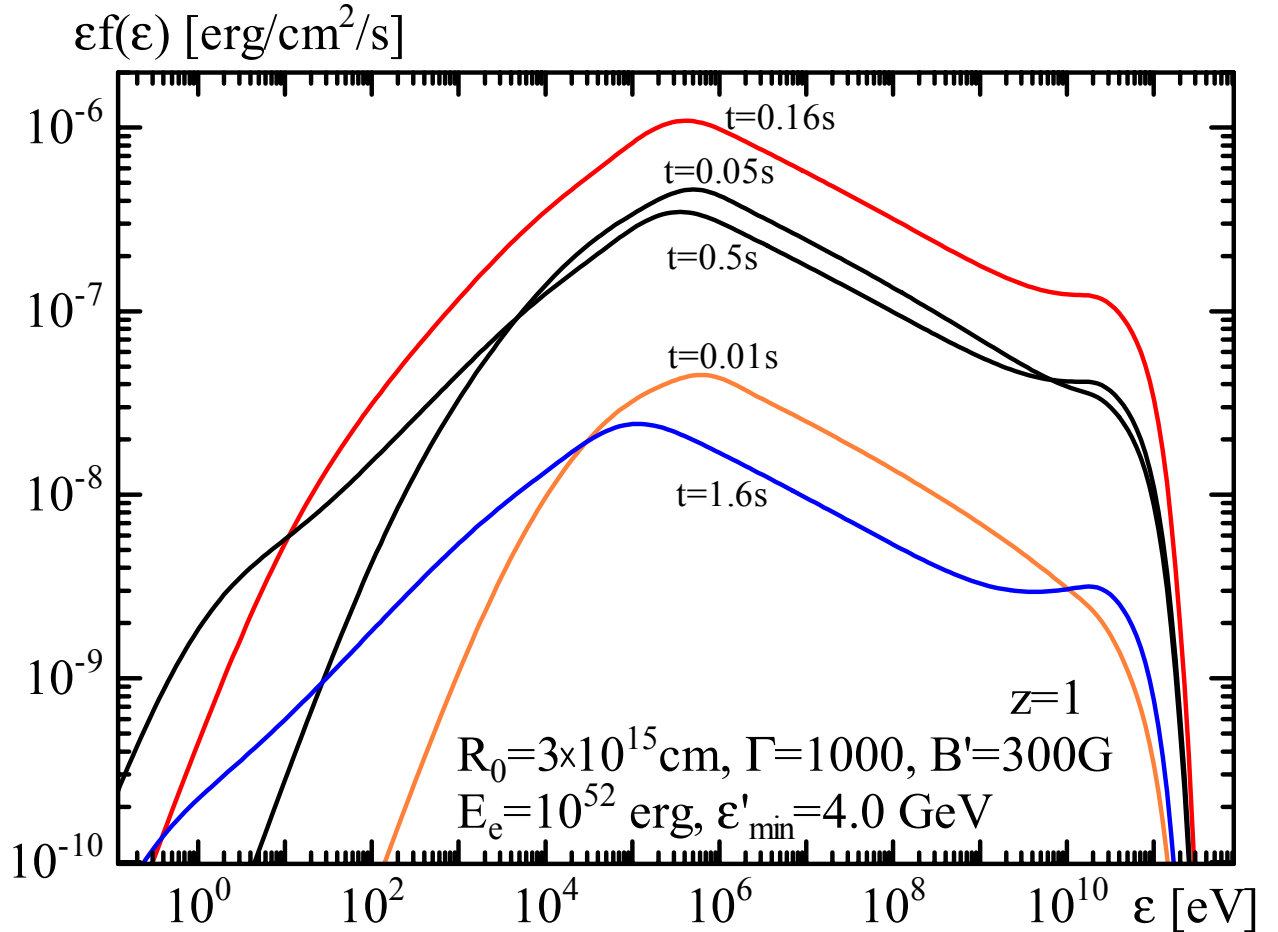

Fig. 5.— Temporal evolution of the observable spectral photon flux for the model Run2 (see also Figure 6). The time-bins are the same as in Figure 6, and the denoted times are the center for each time-bin.
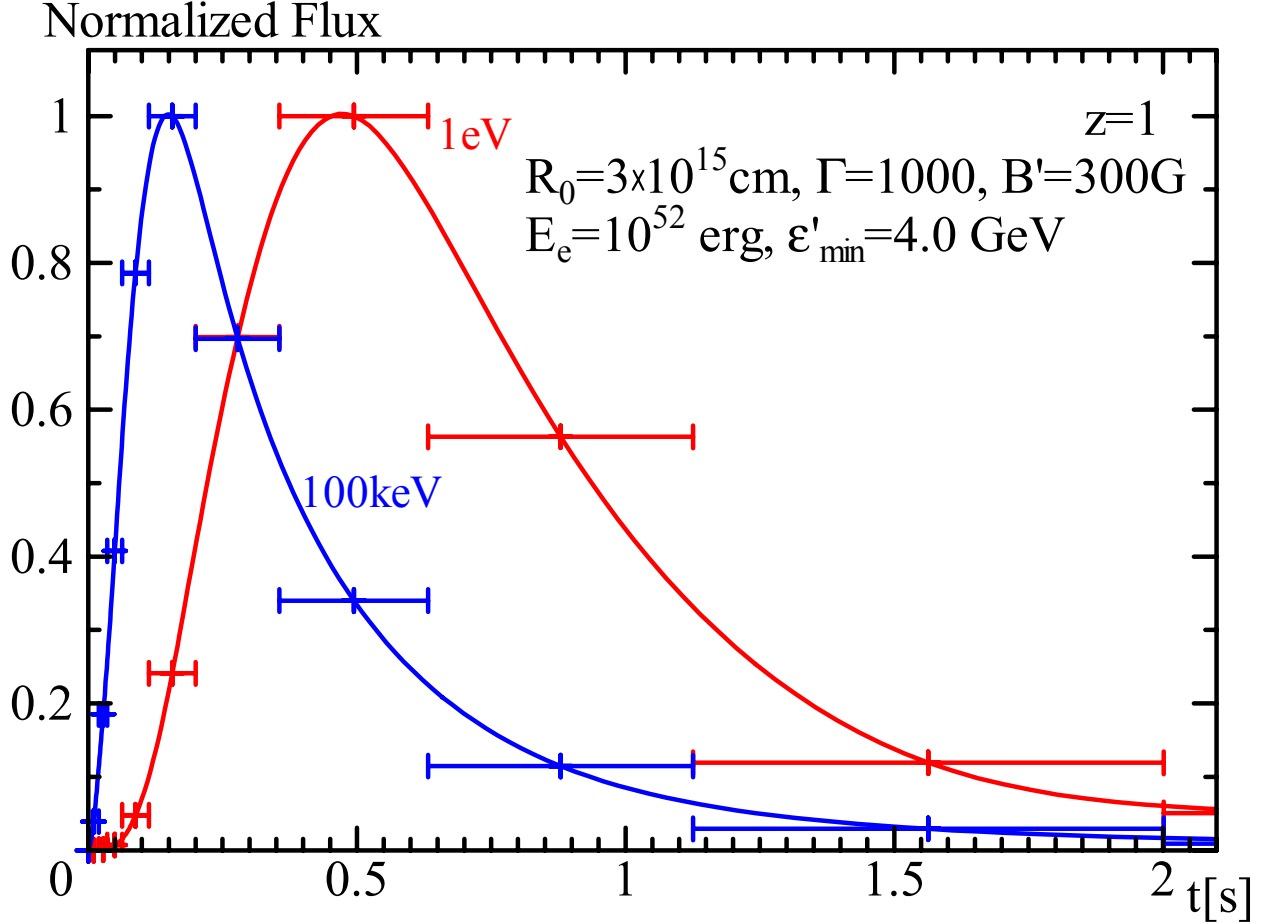
Fig. 6.— The light curves for the model Run2, whose parameters are denoted inside the figure. The plotted values are normalized by the maximum flux. We smoothly join the fluxes averaged over respective time-bins with solid curves for reference.

The time-integrated spectrum for the more compact case of Run3 is similar to that of Run2 (see Figure 4) so that we can expect an optical pulse and 100 GeV photons possibly detectable with Čerenkov detectors such as MAGIC or CTA for those two cases. The high-energy cut-off in the spectrum is mainly due to the internal $\gamma\gamma$-absorption rather than due to the EBL, unlike for the case of Run2. The relatively fast electron cooling due to the high magnetic field in Run3 promptly generates a soft photon spectrum with a photon index ~ -1.5 below $\varepsilon_{\mathrm{peak}}$. Thus, in this case no significant softening is found during the pulse rise phase (< 0.58s) unlikely Run2. On the other hand, the smaller radius than that in the case of Run2 yields a slight evolution of the high energy cut-off due to $\gamma\gamma$-absorption. Therefore, the peak of the 100 GeV light curve appears earlier than that of the lower energy bands, while the light curves for keV-GeV regimes almost overlap with the 100 keV lightcurve. The
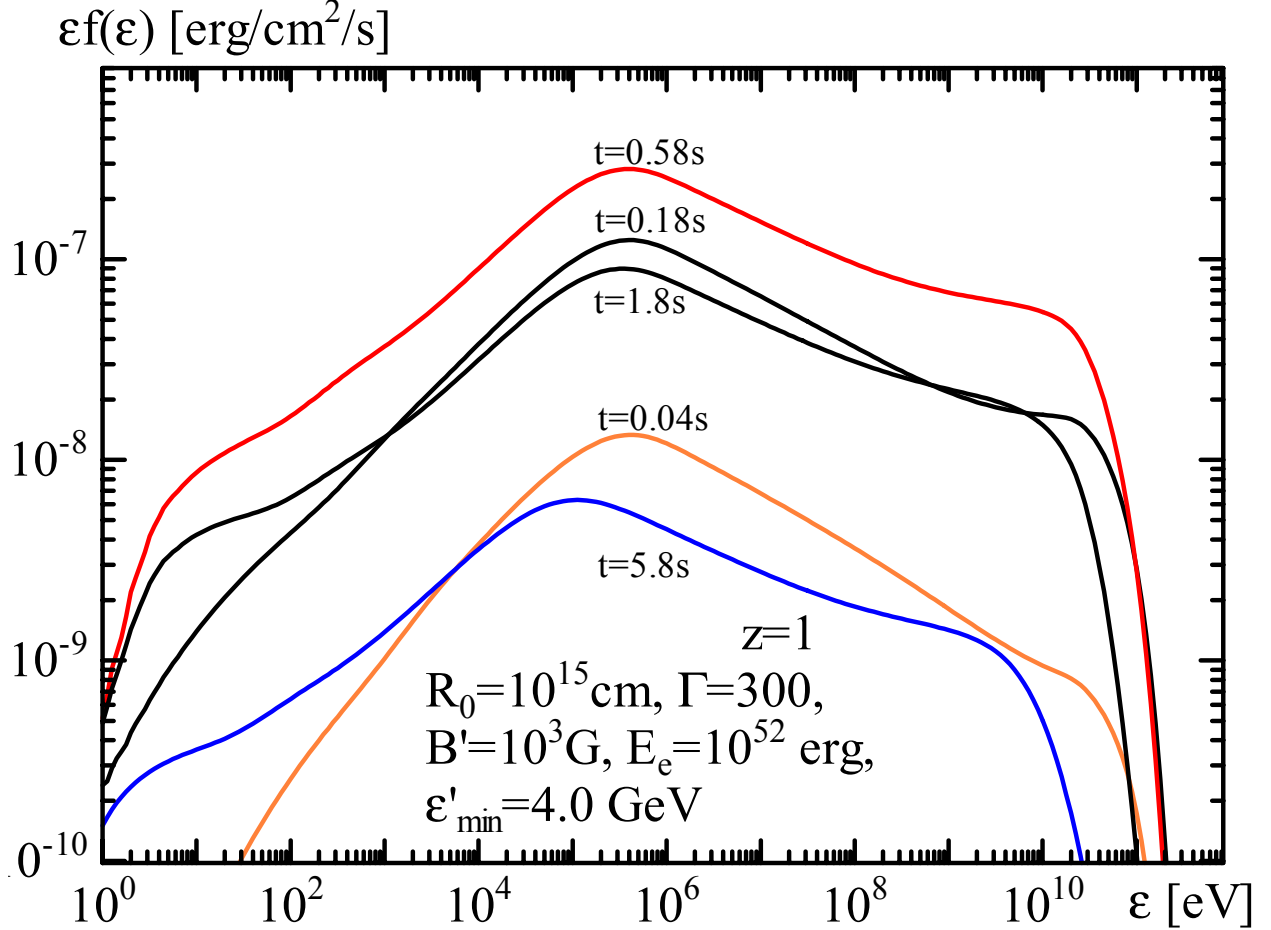
Fig. 7.— Temporal evolution of the observable spectral photon flux for the model Run3 (see also Figure 8). The time-bins are the same as in Figure 8, and the denoted times are the center for each time-bin.

heating of electrons due to SSA (Ghisellini et al. 1988) is so effective that a slight bump appears at a few eV in the spectrum in Figure 4. The high-energy bump, prominent above 100 MeV compared to Run2, may be due to secondary electron-positron pairs produced via $\gamma\gamma$-absorption (Asano & Inoue 2007).

Above the $\gamma\gamma$ cut-off energy, the intrinsic spectral shape for Run3 is well approximated by a power-law rather than by an exponential cut-off. This steep power-law shape is also seen in the spectrum of Run1. If we take into account the spatial structure of the source, a smoothly broken power-law would be expected as a $\gamma\gamma$-absorption signature (Baring 2006; Granot et al. 2008). We see that, even with our one-zone approximation, the temporal evolution of the spectrum generates a broken power-law shape in the time-integrated spectrum.
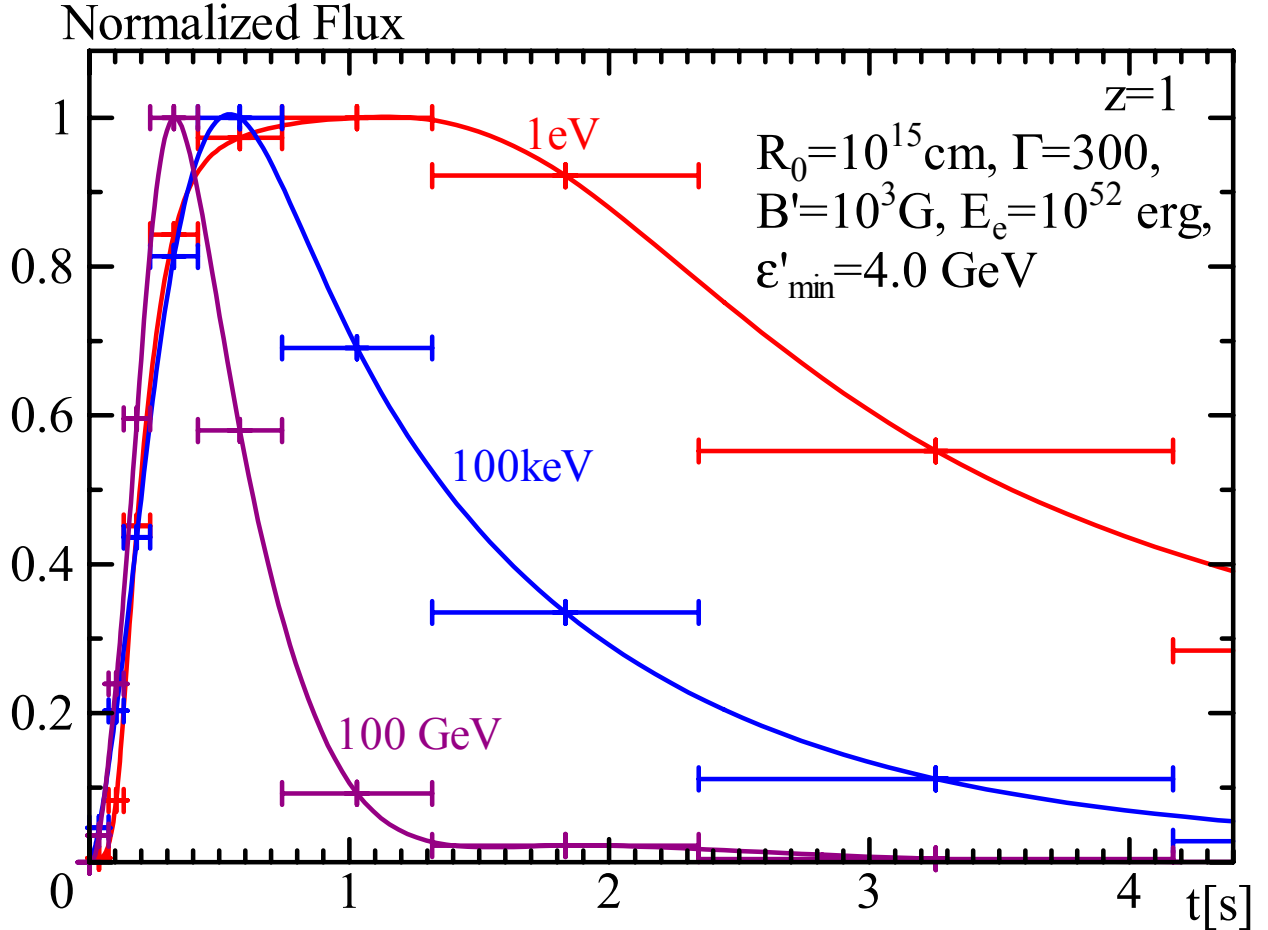
Fig. 8.— Light curves for the model Run3, whose parameters are denoted inside the figure. The plotted values are normalized by the maximum flux. We smoothly join the fluxes averaged over respective time-bins with solid curves for reference.

The poor statistics in the spectral data of GRB 090926A (Ackermann et al. 2011), for which the spectral break is reported around 1.4 GeV, makes it difficult to distinguish whether the spectral shape is one of a broken power-law or an exponential cut-off. Thus, future detections with better statistics are needed of bright bursts with *Fermi* or with Čerenkov telescopes, in order to determine more precisely the spectral shape above the cut-off energy.

Our results show that the curvature effect yields a spectral lag between the optical and the keV-MeV bands. In the keV-MeV energy range, several authors have reported time delays in the arrival time of lower energy photons relative to higher energy photons ("positive lags", e.g., Norris et al. 1996; Wu & Fenimore 2000; Hakkila & Giblin 2004; Chen et al. 2005; Hakkila et al. 2008; Arimoto et al. 2010). These spectral delays may be explained by

the curvature effect (Ioka & Nakamura 2001; Shen et al. 2005; Lu et al. 2006). As Lu et al. (2006) discussed, the curvature effect predicts that a smaller Γ tends to yield a larger lag, i.e., softer photons arrive increasingly later. The optical delay in our results is consistent with this tendency, the smaller Γ in Run3 resulting in a broader 1 eV light curve than that in Run2 (note that the optical delay in Run2 is mainly due to the slower electron cooling). However, the observed energy dependence of the lag does not always follow the prediction of the simple curvature effect (Zhang et al. 2007; Arimoto et al. 2010). We should also take into account the temporal evolution of the spectral shape (Kocevski & Liang 2003; Daigne & Mochkovitch 1998, 2003; Bošnjak et al. 2009). It would be interesting to fit the observed spectral lags by evolving some of the model parameters, such as the magnetic field, although it is not our purpose to discuss such effects in this paper.

The broad pulse profile in the optical band means that the optical pulses tend to overlap each other. The observed broader pulses and longer tail in the optical light curve compared to the gamma-ray light curve in GRB 080319B (Racusin et al. 2008) is consistent with this tendency, although an extra spectral component is required to reproduce the optical flux in that burst. Recalling that the slow electron cooling is a key to the optical lag in Run2, we emphasize that the spectral evolution should be investigated not only in the GeV band but also in the optical band in order to probe the prompt emission mechanism.

3.2. "Fermi-LAT" Case

The *Fermi* satellite detected GeV photons from several very bright bursts ($E_{\rm iso} > 10^{54}$ erg) such as GRB 080916C (Abdo et al. 2009c), GRB 090902B (Abdo et al. 2009b), and GRB 090926A (Ackermann et al. 2011). In such bursts the onset of the GeV emission is delayed with respect to the MeV emission, i.e., they have (in this energy range) negative lags. In addition, some of them also have an extra spectral component above a few GeV, distinct and additional to the usual Band function which dominates in the MeV energy range. As Corsi et al. (2010) discussed, the GeV emission may be due to IC emission from internal dissipation regions. In this subsection we choose a set of parameters, which may be relevant for such bright GRBs accompanied by an additional GeV emission component, although we do not attempt to perform fits to the spectrum of any specific GRB.

In Figure 9, we plot the evolution of the spectral photon density in the shell frame for Run4, in which we have adopted a very large injection energy ($E_{\rm e} = 10^{54}$ erg) and a high Lorentz factor ($\Gamma = 1000$). If we adopt $\epsilon_{\rm e} = 0.5$, $B = 100$ G corresponds to $\epsilon_B = 5.4 \times 10^{-4}$. The Thomson optical depth is low enough, $\tau_{\rm T} = 3 \times 10^{-5}$, even for the large $E_{\rm e}$.
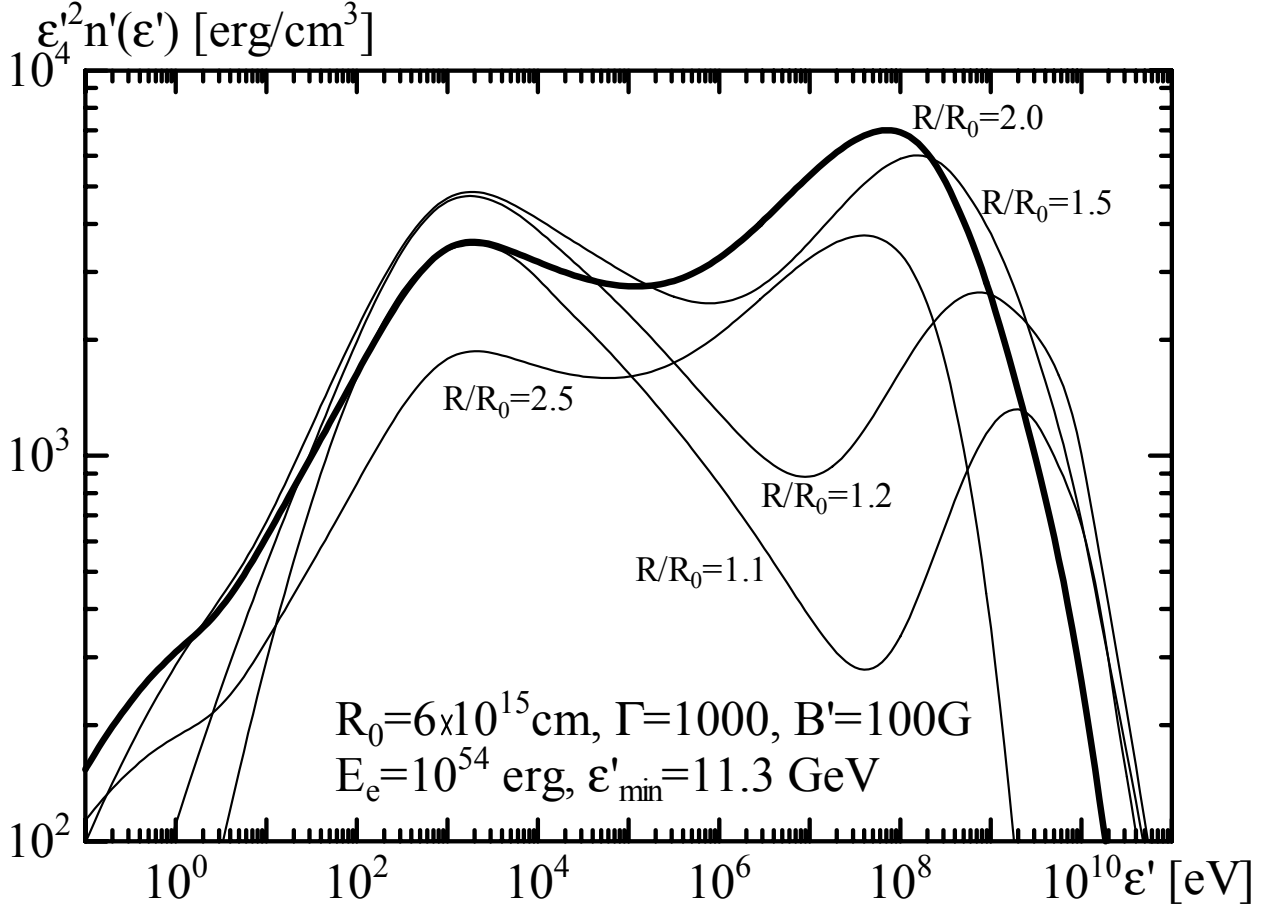
Fig. 9.— Temporal evolution of the spectral energy density of photons in the shell frame for Run4. The model parameters are denoted inside the figure. The electron injection is ended at $R/R_0 = 2.0$ (thick line).

Initially the synchrotron component at $\sim$ keV dominates the spectrum, but the IC component grows as electrons are continuously injected. In the later stage the injected electrons cool mainly via IC rather than synchrotron, so the synchrotron component starts to decay earlier than the IC component. At the end of the electron injection ($R/R_0 = 2$) the cooled electrons are still relativistic, because the energy density of the magnetic field is low (~ 400 erg cm^{-3}). Equating the synchrotron cooling timescale and the dynamical timescale W'/c, the energy of the cooled electrons is

$$
\begin{aligned}
\varepsilon'_{\rm e,cool} &= \frac{6\pi m_{\rm e}^2 c^4 \Gamma}{\sigma_{\rm T} B'^2 R_0} \\
&\simeq 200 {\rm MeV} \left(\frac{B'}{100~{\rm G}}\right)^{-2} \left(\frac{\Gamma}{1000}\right) \left(\frac{R_0}{6\times 10^{15}~{\rm cm}}\right)^{-1}.
\end{aligned}
\tag{28}
$$

The contribution of IC cooling with the Klein-Nishina effect can also be comparable to the above estimate, as the obtained spectra show; the photon energy densities of the IC and synchrotron components are comparable. Actually, our numerical results indicate a spectral bump in the electron distribution around 100 MeV at $R/R_0 = 2$. Even after the end of electron injection, such cooled electrons continue emitting synchrotron photons. The cooling due to IC gradually becomes inefficient as the seed photon density around keV energies decreases. The typical synchrotron photon energy from the cooled electrons is

$$
\begin{aligned}
\varepsilon'_{\gamma,\mathrm{cool}} &= \frac{3\pi\hbar e B'}{8 m_{\mathrm{e}} c} \gamma'^2_{\mathrm{e,cool}} \\
&\simeq 0.2\mathrm{eV} \left(\frac{B'}{100\ \mathrm{G}}\right)^{-3} \left(\frac{\Gamma}{1000}\right)^2 \left(\frac{R_0}{6\times 10^{15}\ \mathrm{cm}}\right)^{-2}.
\end{aligned}
\tag{29}
$$

In the spectra for $R/R_0 = 2$ and 2.5 we can see a spectral bump below ~ 1 eV, which is attributed to the late synchrotron emission from the cooled electrons.

Assuming a redshift $z = 4.35$ such as that of as GRB 080916C, we show the evolution of the spectrum in the observer frame for this Run4 case in Figure 10. The IC component in the GeV-10 GeV range grows with time, and the late synchrotron emission discussed above produces a spectral break at keV $\sim \Gamma\varepsilon'_{\gamma,\mathrm{cool}}$. The spectrum seems to evolve from the initial Band-function to a power-law dominated shape in the later stages. This spectral evolution is interestingly similar to that seen in GRB 090510 (Abdo et al. 2009a; Ackermann et al. 2010), although that burst is a short GRB. The spectrum evolves to a power-law-like shape well after the peak time of the pulse (typically $t = 2.6$ s in Figure 10, see also Figure 13). If many pulses overlap each other, a dominant pulse may prevent the detection of the underlying power-law-like component. Therefore, it is interesting that GRB 090510 is one of the short GRBs, which have only one or two pulses in most cases. In many *Fermi*-LAT GRBs, the spectra tend to evolve toward a simple power-law spectrum extending as far as GeV in the later stage of the prompt emissions. Even for such long GRBs, the spectral evolution seen in our simulation would be applicable, because active pulses may gradually disappear in the later stage. While such spectra may be explained by the early onset of the afterglow (Ghisellini et al. 2010; Kumar & Barniol Duran 2010), a combination of the late synchrotron emission and a decaying IC component can also produce a power-law-like spectrum.

The time-integrated spectrum in Figure 11 shows extra components below keV and above 100 MeV, comparable to those seen in GRB 090510 (Ackermann et al. 2010) and GRB 090926A (Ackermann et al. 2011). To explain the observed extra components that dominates the emission both below 10 keV and above 100 MeV, a single contribution from an IC component is not sufficient. However, the late synchrotron emission can assist in
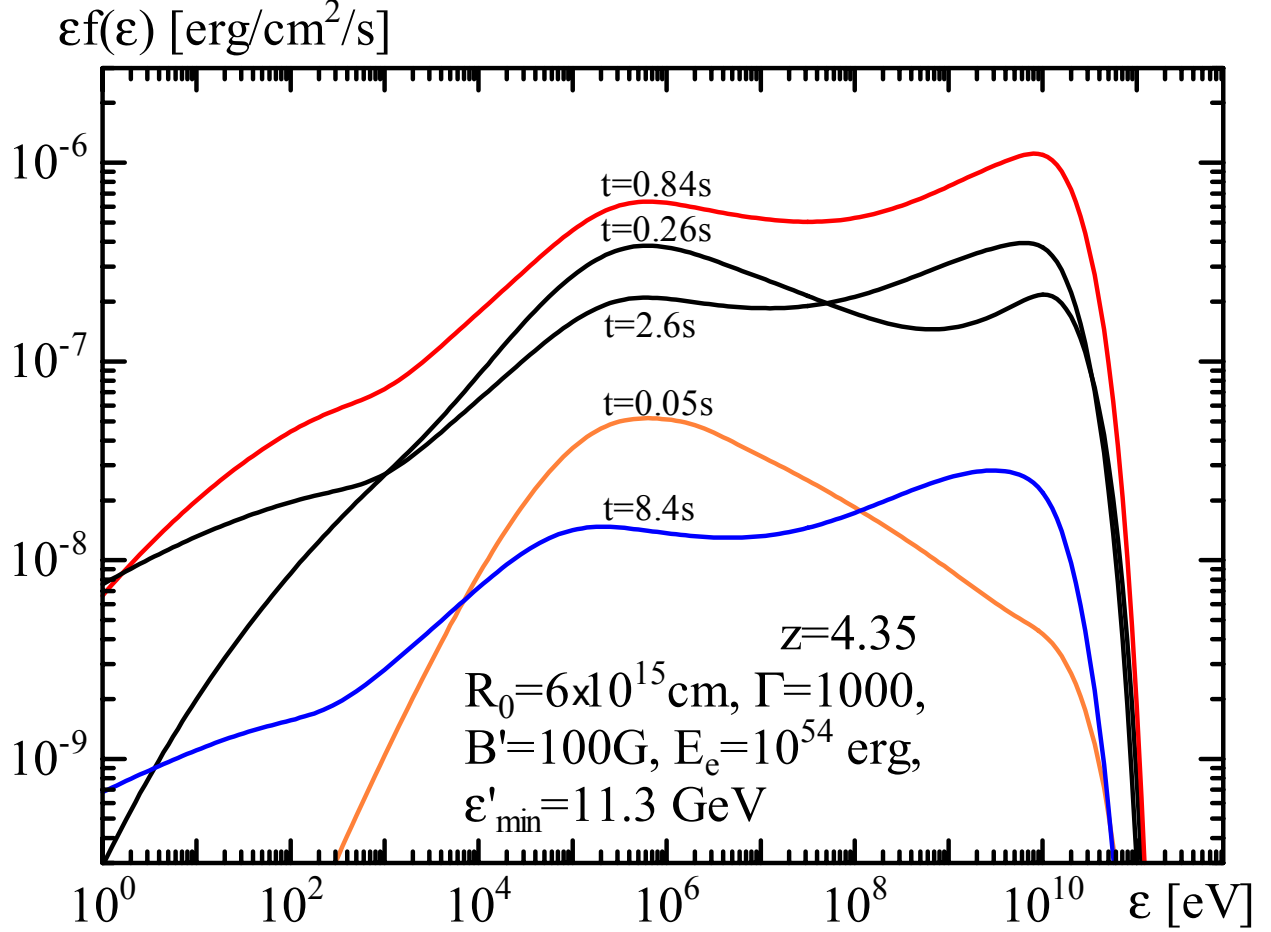
Fig. 10.— Temporal evolution of the observable spectral photon flux for the model Run4 with $z = 4.35$. The time-bins are the same as the logarithmic time-bins in Figure 13, and the denoted times are the center for each time-bin.

extending the extra component into the lower energy range, as shown in Figure 11. It seems that a single power-law component with a photon index -1.82, which is close to the index -1.79 in GRB 090926A, overlaps the usual Band function that dominates the emission around MeV, despite the fact that the two spectral excesses in the low and the high energy regions have different physical origins.

In Figure 12 we plot the light curves based on the spectral flux with linear time-bins, in order to distinguish the peak times. The light curves show a delayed onset of the optical emission, which is partially due to the late synchrotron emission. The late growth of the IC emission makes the growth of the early GeV light curve slower compared to the 100 keV emission (see also Bošnjak et al. 2009), the GeV peak time appearing delayed ~ 0.4 s
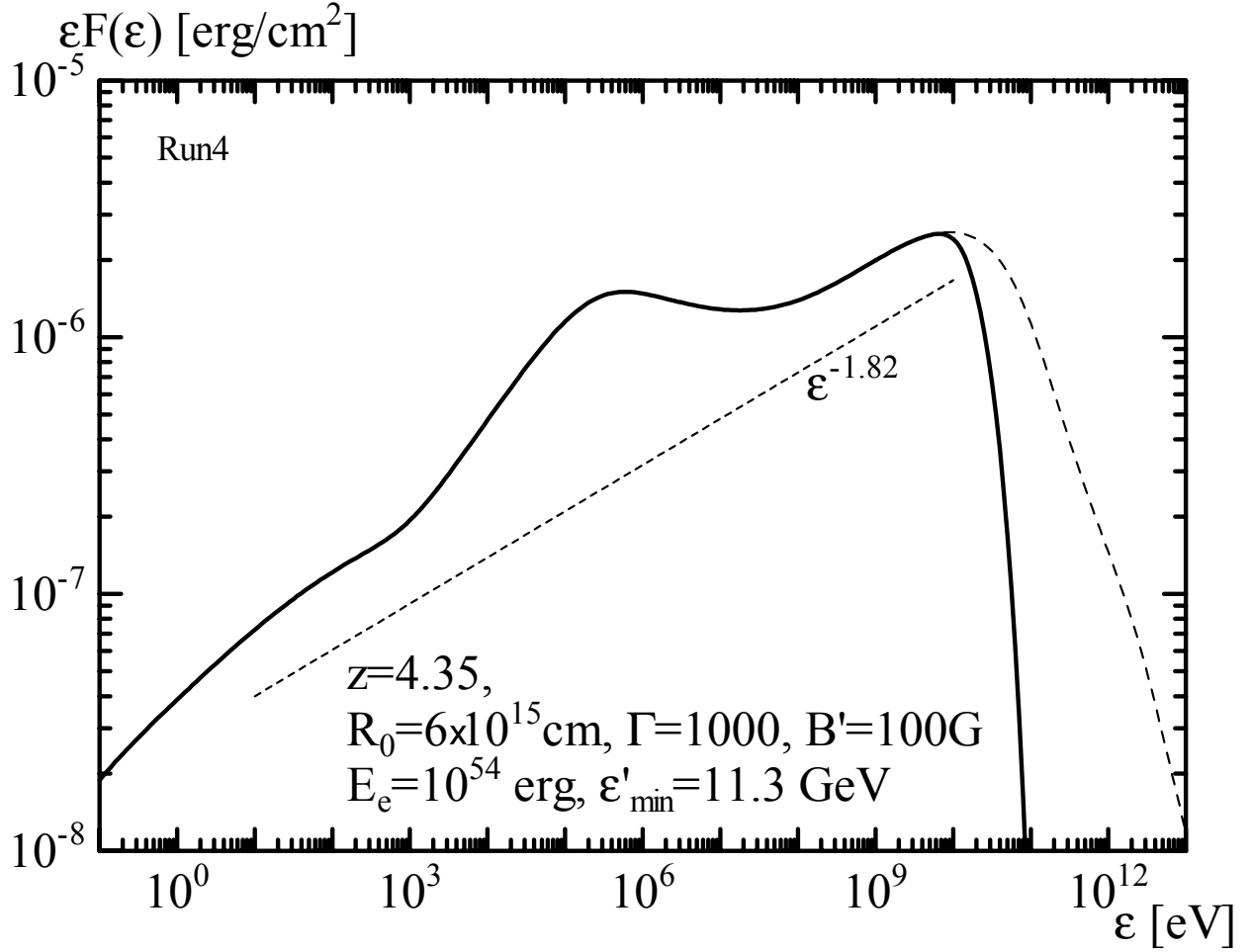
Fig. 11.— Time-integrated observable flux for Run4 with $z = 4.35$. The dashed lines denote the cases neglecting $\gamma\gamma$-absorption due to EBL.

relative to the 100 keV peak time. One needs however to take into account the low photon statistics above 100 MeV in the GRB observations with *Fermi*. Thus, in Figure 13 we plot the expected photon-count rates integrating over the 100 MeV - 1 GeV and the > 1 GeV ranges. Here we have simply assumed constant effective areas of 3,000 cm^2 and 7,000 cm^2 for energies below and above 1 GeV, which mimic the effective are of the *Fermi*-LAT detector (Rando et al. 2009). While the count rates with logarithmic and linear binning give us rather different impressions, the figure shows that we expect from this simple one-zone SSC model a detection of one photon with the *Fermi*-LAT, delayed at least ~ 1 s after the onset of the 100 keV or MeV emission. On the other hand, the observed delay of the GeV emission seen in GRB 080916C is ~ 4 s, which is substantially longer than 1 s. Although the GeV delay due to the growth of the IC component would be within the approximate timescale of
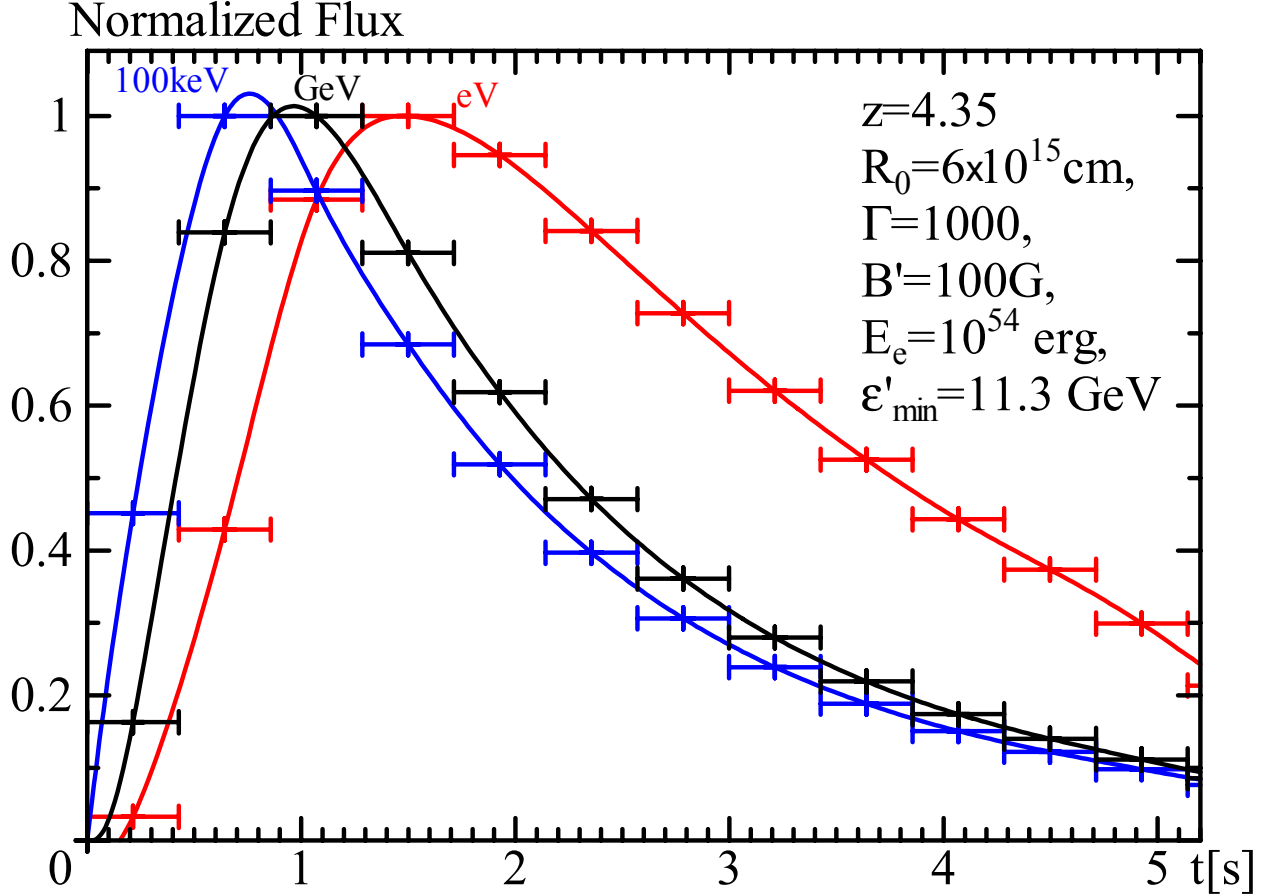
Fig. 12.— Light curves for the model Run4 with $z = 4.35$ based on the spectral flux. The time-bins are linearly divided. The plotted values are normalized by the maximum flux. We smoothly join the fluxes averaged over respective time-bins with solid curves for reference.

the keV-MeV pulse width, this delay appears able to explain only a fraction of the observed delayed onsets of the GeV emission in long bursts.

3.3. External Photons

As discussed in the last subsection, the IC emission tends to be delayed relative to the main keV-MeV emission, but the longer delay than the pulse timescale of the MeV emission such as observed in GRB 080916C (Abdo et al. 2009c) is not explained by this effect only. As a possible solution, Toma et al. (2009, 2010) pointed out that the delayed GeV onset can be reproduced by the introduction of external photons such as the X-ray emission from
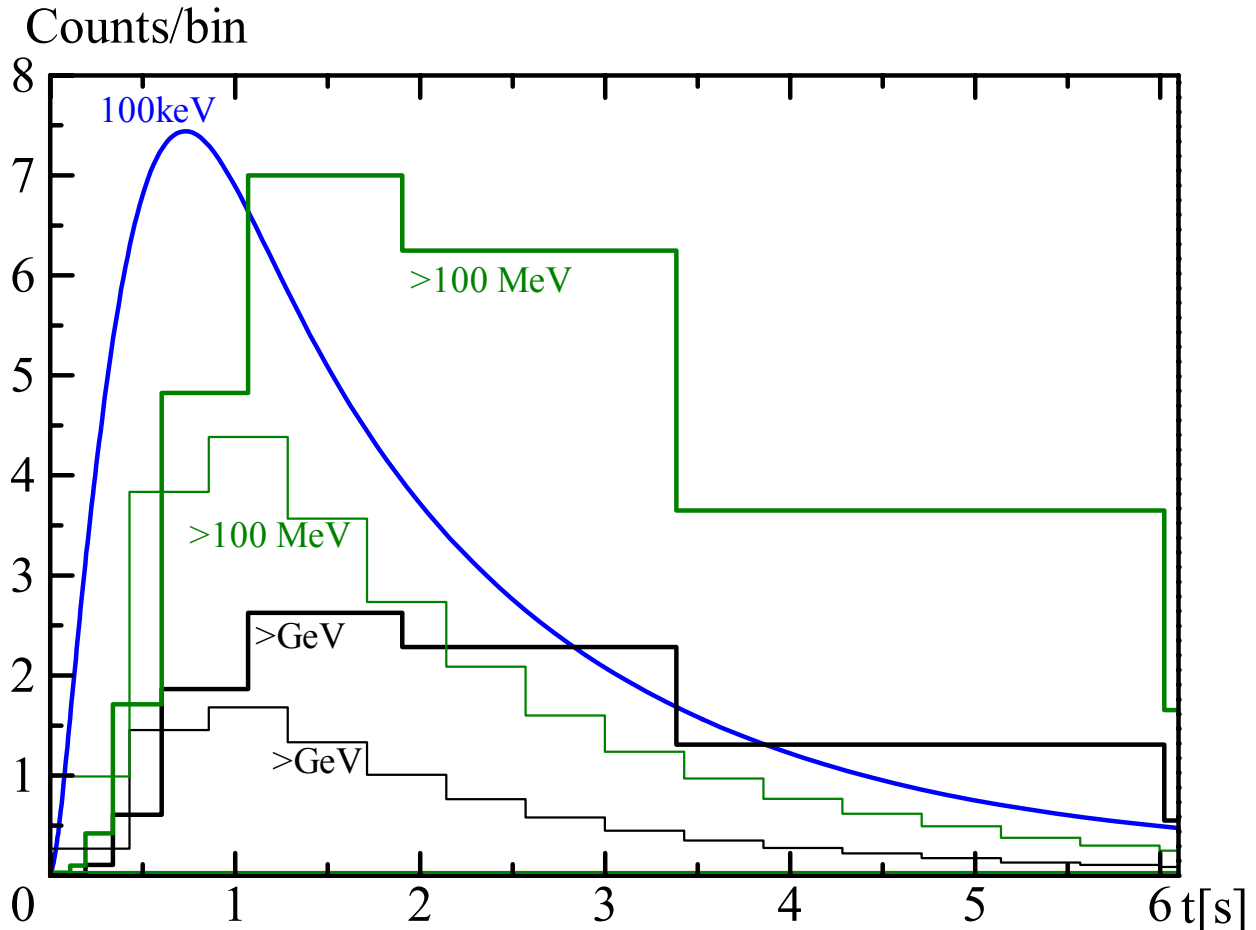
Fig. 13.— Expected photon counts per each time-bin above 100 MeV and GeV for the model Run4 with $z = 4.35$. The thick (thin) histograms correspond to logarithmic (linear) time-bins. For comparison we also plot the 100keV-lightcurve (arbitrary unit), whose shape is the same as that in Fig. 12.

the cocoon (see also Li 2010; Murase et al. 2011). The geometrical configuration in those models, namely the spatial separation between the source of the external photons and the site of the internal shock or generic dissipation region can cause the delayed arrival of the up-scattered external photons. In particular, the photospheric emission (Paczýnski 1986; Mészáros & Rees 2000) can provide the external seed photons for the IC emission from electrons accelerated in regions outside the photosphere. As suggested, e.g., for GRB 090902B (Ryde et al. 2010; Zhang et al. 2011), many authors have discussed the photospheric emission as the main MeV component.

In this subsection we assume that a quasi-steady emission provides the main MeV

component, emanating from an inner region, while an outside dissipation region producing accelerated particles upscatters these photons, as Toma et al. (2010) assumed. The quasi-steady emission may originate from the photospheric emission, but we do not specify its origin here. The model details are as follows: The spectral shape of the quasi-steady emission is a Band function (Band et al. 1993), whose parameters are the luminosity $L_{\rm seed}$, peak energy $\varepsilon_{\rm peak}$, and spectral indices α and β. Here, the external emission is assumed to start at a time $\sim R_0/c$ before the electron injection. In this Band photon field, accelerated electrons are injected in a shell expanding from $R = R_0$ in the same way as we did in the previous subsections. In the shell frame, the external photon field should be anisotropic, because the Band component may be emitted (depending on the specific model) from a radius $\ll R_0$, and its source may have a different bulk Lorentz factor than the Γ of the shell. Although our one-zone numerical code cannot fully include the effects of such an anisotropy, we endeavor to take it into account partially as follows. As long as the electron distribution in the shell frame is isotropic, the total IC emissivity, even for anisotropic seed photons, is written with the average intensity of the seed photons as

$$J(\varepsilon_\gamma) \equiv \frac{U_{\rm seed}(\varepsilon_\gamma)c}{4\pi} \qquad (30)$$

(Aharonian & Atoyan 1981; Brunetti 2000), where $U_{\rm seed}(\varepsilon_\gamma)$ is the spectral energy density of the seed photons. However, reflecting the distribution of the seed photons, the resultant emissivity also becomes anisotropic. If the seed photons are emitted from a radius $\ll R_0$, we can consider highly beamed seed photons that radially propagate even in the shell frame. In this case the anisotropy in the IC emissivity may be approximately included by adding an extra factor $(1 - \cos\theta')$ in Eq. (21) in the Thomson limit (Wang & Mészáros 2006; Fan et al. 2008; Toma et al. 2009). This is because electrons moving in the same direction as the photon beam have a smaller probability to interact with those photons, while conversely the head-on collisions between electrons and photons is much more efficient. In this approximation the IC emission becomes maximum from the marginally high-latitude surface of the shell, rather than from the on-axis surface. For a totally beamed photon field, its spectral shape in the shell frame is obtained by shifting the above Band function to a lower energy by a factor of $(1 + \beta_{\rm sh})\Gamma$. The average intensity of the Band component in the shell frame is calculated with a normalization of the energy density

$$\int d\varepsilon'_\gamma U'_{\rm seed}(\varepsilon'_\gamma) = \frac{L_{\rm seed}}{4\pi c R^2 (1 + \beta_{\rm sh})\Gamma^2} \propto R^{-2}, \qquad (31)$$

for the totally beamed case. This provides an extra factor $(1+\beta_{\rm sh})$, compared to the isotropic seed-photon case.

The results shown below are obtained with the fully-beamed approximation mentioned above. While expedient and useful, some of the weaknesses of such an approach are listed for
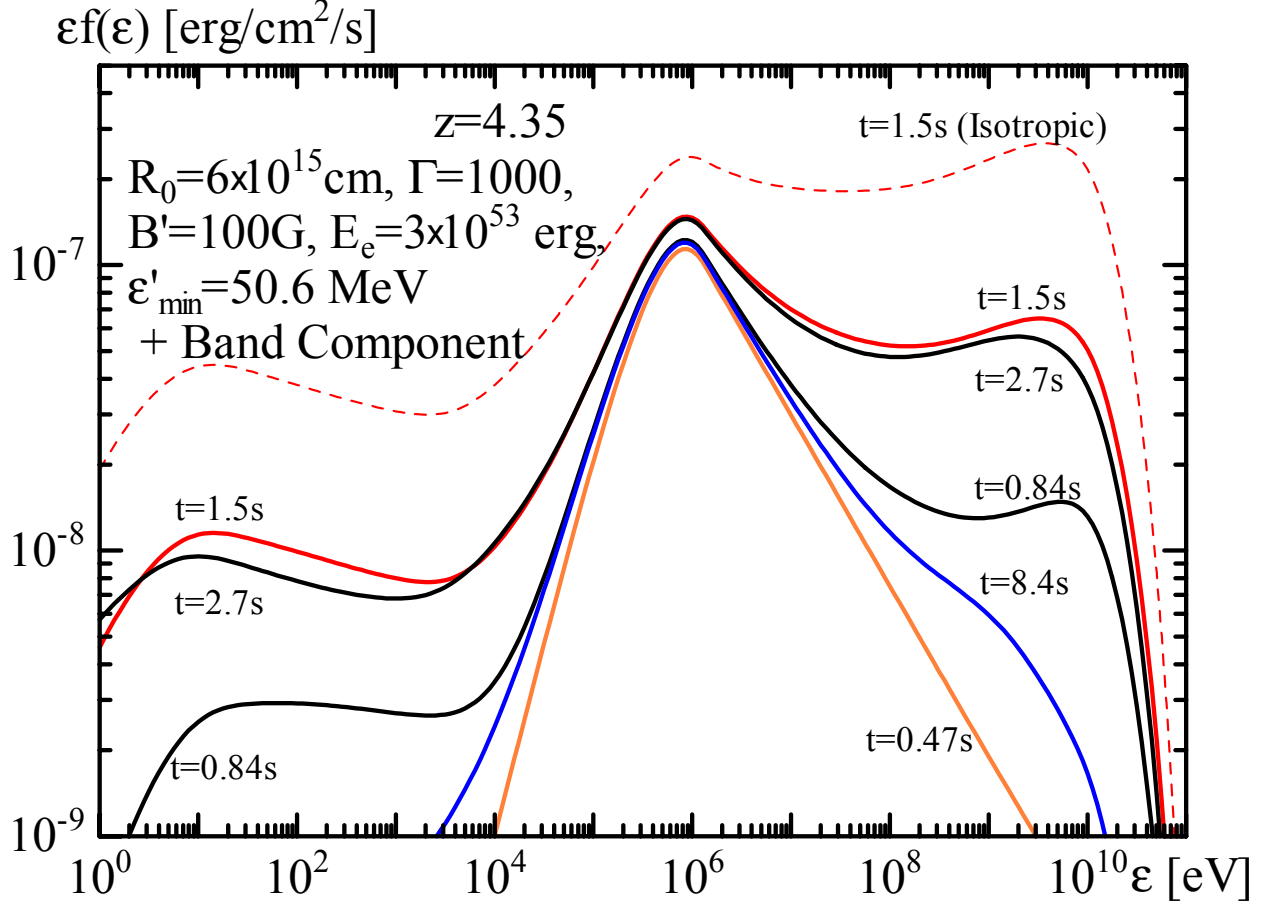
Fig. 14.— Temporal evolution of the observable spectral photon flux for the model Run5 including the external Band component with $z = 4.35$. The model parameters are denoted inside the figure. The fluxes are averaged over the logarithmic time-bins in Figure 15 and the denoted times are the center for each time-bin. The solid lines are calculated based on the fully-beamed approximation, while the thin dashed line represents the results in the isotropic approximation.

completeness below. The method in our code corrects for anisotropic effects all of the emissions from the shell, including synchrotron, which should be independent of the anisotropy of the extra photon field. Moreover, the seed photons for the IC include not only the external Band component but also the photons emitted in the shell itself (SSC or secondary IC emissions). Such secondary seed photons may soften the IC anisotropy. The Klein-Nishina effects may also result in deviations from a simple anisotropic factor $(1 - \cos \theta')$. Even if the anisotropy of the emissivity in the shell is simply expressed by this factor, the θ'-dependence of the escape timescale should yield the temporal evolution of the anisotropy of photon distri-

bution. Photons with small $|\cos\theta'|$ remain in the shell longer than photons with $|\cos\theta'| \sim 1$. Thus, the angular distribution should evolve even for the constant angular dependence of the emissivity. Nevertheless, the one-zone and fully-beamed approximations force the angular distribution to remain as $(1 - \cos\theta')$. Given the average photon energy $\overline{\varepsilon_\gamma}$ in the shell, our treatment results in the average momentum of the escaped photons to become $-\overline{\varepsilon_\gamma}/(2c)$, although that of the photons in the shell is $-\overline{\varepsilon_\gamma}/(3c)$. Owing to the negative average momentum, the fluence for the observer decreases by a factor two compared to the isotropic approximation.

The anisotropy of the Band component may affect $\gamma\gamma$-absorption as well (Zou et al. 2011; Zhao et al. 2011). The high-energy cut-off can be higher than that calculated here. In this case too, however, the target photons against $\gamma\gamma$ are not only the external photons. Since in any case our one-zone approximation is not suited for including the effect of the anisotropy in the absorption, we do not include these effects here.

We adopt the parameters of the Band spectrum as $L_{\text{seed}} = 10^{53}$ erg s^{-1} and $\varepsilon_{\text{peak}} \simeq 1$ MeV in the observer frame, $\alpha = -0.6$, and $\beta = -2.6$ in the simulations of Run5 (Figures 14 and 15). The parameters for the internal shock are similar to those in Run4 except for a small $\varepsilon'_{\text{min}}$ (if $\epsilon_{\text{e}} = 0.5$, $\epsilon_B = 0.0018$; $\tau_{\text{T}} = 2 \times 10^{-3}$). The small $\varepsilon'_{\text{min}}$ leads to a large implied proton energy. The proton density n'_{p} would be the same as the electron density estimated from Eq. (27). Even if we neglect the thermal energy, the proton energy $E_{\text{p}} \sim \Gamma m_{\text{p}} c^2 n'_{\text{p}} V' \sim 1.9 \times 10^{54}$ erg is fairly large. In Figure 14 we show the spectral evolution for the observer. We see that the synchrotron and IC emission in the shell contributes to a wide energy range, while the Band component is prominent mainly in the MeV range.

In Figure 15 we show the corresponding light curves. We see that the GeV and eV emissions originating from the (outer) shell are delayed $\sim (1 + z)R_0/\Gamma^2/c \sim 1$ s relative to the MeV emission, which is "external", i.e., it originates from a region which is at smaller radii than the shell. We should note that the start time of this external emission can be arbitrary adjusted, depending on the model, so that the delay timescale could be longer than shown by our results. Since we assume a quasi-steady Band component, the MeV emission continues even after the end of the GeV emission. For comparison, we have also plotted in Figure 15 the light curves using the isotropic approximation for the photon emissions (thin lines). Since the marginally high-latitude emission contributes the most to the flux in the fully-beamed approximation, the light curves show larger delayed onsets and longer tails relative to those in the isotropic cases (~ 0.3 s). The Lorentz boost of the anisotropic emissions reduces the fluence to half of that of the isotropic emission owing to the negative average photon momentum in the shell frame. Thus, those lower fluences and longer emission timescales in the fully-beamed approximation result in the lower fluxes shown in Figure 14.
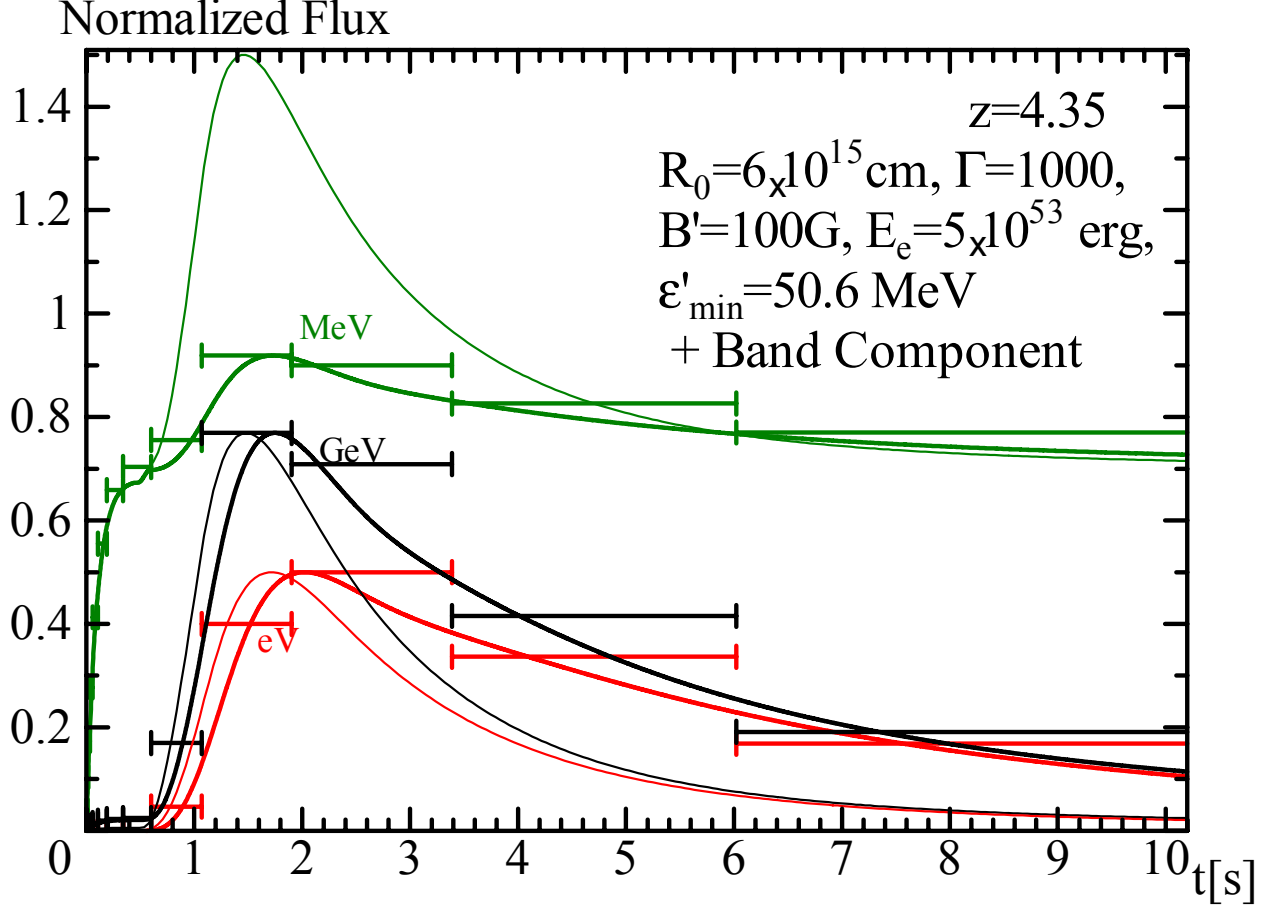
Fig. 15.— Light curves for the model Run5 including the external Band component with $z = 4.35$ based on the spectral flux. The normalizations are arbitrarily shifted to un-merge the lines. The solid lines are plotted based on time-bins linearly divided (0.0423 s). The fluxes averaged over logarithmic time-bins are also plotted. The fully-beamed and isotropic approximations are given by the thick and thin lines, respectively. The peak fluxes for the thick and thin lines are aligned in the GeV and eV light curves, while the MeV light curves are normalized with the external photon flux.

The origin of the eV emission is basically synchrotron, so the light curve in the isotropic approximation (thin line) may be more appropriate for this. Even for the IC emission, the actual flux evolution may be between the cases represented by the fully-beamed and the simple isotropic approximation.

The internal shock produces the synchrotron and IC components at ~ 10 eV and ~ 10 GeV, respectively. The synchrotron peak appears able to explain the optical extra component observed in GRB 080319B (Racusin et al. 2008). In the later stages, the seed photons for

the IC process are not only the Band component but also shell synchrotron photons, so the IC emission contributes to 100 keV range as well as to the 10 GeV range. As a result, the photon indices for the Band function below a few MeV evolve to $\alpha \simeq -1.25$ and $\beta \simeq -2.35$ near the peak flux ($\alpha \simeq -1.52$ and $\beta \simeq -2.13$ for the isotropic approximation) and return to the initial values later. Similarly, the spectrum in GRB 080916C becomes flat in $\varepsilon f(\varepsilon)$-plot, when the GeV emission brightens (Abdo et al. 2009c). Thus, an internal shock with an external Band/photospheric component appears generically able to explain the delayed onset of the GeV emission and the spectral evolution observed in Fermi LAT GRBs.

While almost all the injected energy is released as photons in the former cases of Run1-Run4, the small $\varepsilon'_{\min}$ in Run5 leads to a slower energy release. Within the observer time < 6 s, 79% of the injected energy is released in the isotropic approximation. The integrated energy until the observer time $100(1+z)R_0/\Gamma^2/c \sim 100$ s is 91% of the injected energy (we follow the photon emission from $R = R_0$ to $100R_0$). The rest of the energy is dissipated mostly via adiabatic cooling.

4. Summary of the numerical results

The results of our time-dependent simulations for the internal dissipation model are summarized as follows.

- The temporal evolution of the photon energy distribution inside the shell affects the resultant spectra seen by the observer. Especially for weak magnetic fields, the evolution of the IC component shows the limitation on the steady state approximation. Time-resolved spectra are necessary in order to verify expected features of the spectral evolution, such as the decrease of the cut-off energy due to $\gamma\gamma$-absorption, the growth of the IC component, and a spectral softening due to electron cooling.

- Even in our one-zone approximation, the power-law spectrum is produced above the $\gamma\gamma$ cut-off energy. The spectral evolution and photon escape during the electron injection are essential for this spectral shape.

- We confirm that the light curves follow the FRED shape (Fenimore et al. 1996). The pulse widths and peak times are affected by not only the curvature effect but also the intrinsic evolution of the energy distribution. The decrease of the cut-off energy leads to an earlier GeV peak time, and the gradual electron cooling causes the delayed onset and broad pulse profile of the optical emission.

- The possible deviation mechanisms from the simple Band function (other than IC

emission) are synchrotron emissions from secondary electron-positron pairs, electron heating via SSA, and late synchrotron emission after the injection ends. The latter two mechanisms yield a spectral bump in the low energy portion, while the secondary pairs enhance the synchrotron flux in the high energy range.

- The retarded growth of the IC component can cause the delayed onset of GeV emission. This may be a partial reason for the delayed onsets seen in the *Fermi*-LAT GRBs.

- The combination of the IC and late synchrotron components can produce the "extra spectral component" from keV to GeV as seen in the *Fermi*-LAT GRBs. This is a counter example to the claim that the IC emission cannot explain the extra components in the *Fermi*-LAT GRBs.

- When the IC and late synchrotron components are prominent, a spectral evolution from the Band function to a power-law dominated shape is seen. This is similar to the spectral evolution observed in GRB 090510.

- We confirm the essential features of external photon models such as proposed by Toma et al. (2009, 2010). The IC emission using external Band photons coming from inside regions can reproduce the delayed onset of GeV emission. The effect of the anisotropic emissivity adds an extra factor for the delay timescale. The evolution of the spectral indices is similar to those seen in GRB 080916C. The long-lasting tail of GeV emission in this model is also an interesting feature for the *Fermi*-LAT GRBs.

5. Discussion

Internal shocks, or more generally internal dissipation, have been considered as the main source to explain the GRB prompt emission (Piran 2005; Mészáros 2006), but several problems, such as the narrow distribution of the peak energy $\varepsilon_{\mathrm{peak}}$ (Preece et al. 2000) etc., have led to consideration of photosphere models (Paczýnski 1986; Mészáros & Rees 2000), in which most of the outflow energy is released as thermal photons from the photosphere. More recently, dissipative photosphere models have been invoked to explain the spectra and high efficiency in the prompt emission (Giannios & Spruit 2007; Ioka at al. 2007; Pe'er 2008; Ryde et al. 2010; Beloborodov 2010; Zhang et al. 2011; Vurm et al. 2011). However, internal dissipation regions located outside the photosphere, including the classical internal shock model, are still attractive, as summarized in §4. The emission from accelerated electrons in the dissipation region provides a natural mechanism for emitting GeV photons as detected with *Fermi*-LAT (as for the dissipative photosphere models, see, e.g., Beloborodov 2010; Vurm et al. 2011). Also for the light curve shape, the photospheric radius may be

much smaller than $ct_{var}\Gamma^2$ (t_{var} is the variability timescale), so that the photosphere model must attribute the broad pulse shape to the long-duration activity of the central engine. On the other hand, the internal dissipation models can easily reproduce the FRED shape (Kobayashi et al. 1997) and the spectral lags (Shen et al. 2005). Although some fraction of GRBs such as GRB 090902B may be explained with a simple photospheric component (Zhang et al. 2011), the internal dissipation in the outflows can play an important role not only inside the photosphere but also outside.

In this paper we test two models for the extra-spectral components detected with *Fermi*-LAT; the first is the simple IC emission from accelerated electrons and the second is the up-scattering of external photons. Both models require an internal dissipation region in the outflow, where electron acceleration occurs. The possible delay time in the simple IC model is within the pulse width, so in this model one needs some additional reason to explain the ~ 4 s delay in GRB 080916C. However the external photon model has the additional advantage of being able to reproduce such delayed onsets of the GeV emission. We note that external shock models with a high bulk-Lorentz factor (Ghisellini et al. 2010; Kumar & Barniol Duran 2010) can naturally explain the delayed onset of GeV emission, but as Maxham et al. (2011) have pointed out, the early-phase energy output estimated from the GBM data are not sufficient to explain the GeV fluxes in the prompt phase (see also, He et al. 2011). The variability of the GeV emission needs to be tested with much high photon statistics in order to verify whether their origin is internal or external.

The cascade emissions initiated by hadronic interactions (e.g., Böttcher & Dermer 1998; Gupta & Zhang 2007; Asano & Inoue 2007; Asano et al. 2009b) are also one of the interesting options for explaining the GeV photon emission, related to the potential role of GRB as sources of ultra high-energy cosmic rays (UHECRs) (Waxman 1995; Vietri 1995) and neutrino emission (Waxman and Bahcall 1997; Guetta et al. 2001; Murase & Nagataki 2006). In particular, the flat spectrum of the extra component in GRB 090902B is well explained by the hadronic model with a fiducial parameter set (Asano et al. 2010). However, that GRB may be an exceptional case; the detection of GeV photons generally requires a large bulk Lorentz factor and large emission radius to avoid the internal $\gamma\gamma$-absorption. Such situations reduce the efficiency of the photomeson production. As Asano et al. (2009a) showed, a much larger proton luminosity than gamma-ray luminosity is required to produce the extra spectral component in GRB 090510. Although the high proton loading of the hadronic models is favorable for the GRB-UHECR scenario, the leptonic models considered in this paper are energetically less demanding and appear to provide a broader agreement with the observed spectra and time delays. The spectral evolution in the GeV-TeV range could provide essential clues for distinguishing the leptonic and hadronic models. This paper is thus both a test of purely leptonic GRB models based on SSC and EIC schemes, and also

a first step toward developing a time-dependent code to simulate emissions including the hadronic processes. We plan to compare the evolutions of the GeV-TeV spectrum for both the leptonic and hadronic models in near future.

Concerning the classical internal shock model, in this paper we have not focused on the various problems mentioned with these, which have served as a motivation for photosphere models. We note that the minimum energy of electrons $\varepsilon'_{\min}$, (conventionally expressed by the energy and number fractions of accelerated electrons) is treated as a free parameter in our simulations. Thus, our results do not address questions regarding the narrow distribution of $\varepsilon_{\mathrm{peak}}$ or the empirical $\varepsilon_{\mathrm{peak}}$-correlations such as the Yonetoku relation (Yonetoku et al. 2004). Similarly, the open problem of the low-energy spectral index α is not addressed here. In our results in §3.1 and 3.2 the shorter cooling time than the dynamical timescale makes $\alpha \simeq -1.5$, while the typical observed value is $\alpha = -1.0$ (Preece et al. 2000). To solve the α-problem, several mechanisms have been proposed, such as the Klein-Nishina effect on SSC (Derishev et al. 2001; Bošnjak et al. 2009; Nakar et al. 2009; Wang et al. 2009) and the decay of magnetic fields (Pe'er & Zhang 2006), as well as the effect of the superposition of different optical depth and temperature regions in photospheric models, e.g., Beloborodov (2010) and Vurm et al. (2011). Other issues related to the magnetic geometry and expansion dynamics or to nuclear collisions effects (e.g., Mészáros & Rees 2011) can affect the location of the photosphere or provide additional delay mechanisms. Also, in the dissipation region, we can expect magnetic turbulence due to the Kelvin-Helmholtz instability (Zhang et al. 2009) or the Richtmyer-Meshkov instability (Mizuno et al. 2011; Inoue et al. 2011). Such highly disturbed long-wave magnetic fields may interact with high energy electrons. The electron heating due to the turbulence may harden the spectrum (Asano & Terasawa 2009). Such effects expected in the dissipation region should be considered.

The code discussed in this paper will be further developed to treat hadronic processes as well. In the near future, we plan to carry out simulations for various situations involving dissipative photospheres and internal or external dissipation or shock regions. In order to test with these a realistic picture of GRB, such calculations will need to adopt a wide range parameter sets for the magnetic field, bulk Lorentz factor and baryon loading (see e.g., Ioka 2010; Ioka at al. 2011). Moreover, the code will be useful for simulating emissions of other high-energy sources, such as active galactic nuclei, supernova remnant, and clusters of galaxies.

REFERENCES

Abdo, A. A. et al. 2009, Nature, 462, 331

Abdo, A. A. et al. 2009, ApJ, 706 L138

Abdo, A. A. et al., 2009, Science, 323, 1688

Ackermann, M. et al., 2011, ApJ, 729, 114

Ackermann, M. et al., 2010, ApJ, 716, 1178

Aharonian, F. A., & Atoyan, A. M., 1981, Ap&SS, 79, 321

Arimoto, M. et al., 2010, PASJ, 62, 487

Asano, K. 2005, ApJ, 623, 967

Asano, K., Guiriec, S., & Mészáros, P. 2009, ApJ, 705 L191

Asano, K., & Inoue, S. 2007, ApJ, 671, 645

Asano, K., Inoue, S., & Mészáros, P. 2009, ApJ, 699, 953

Asano, K., Inoue, S., & Mészáros, P. 2010, ApJ, 725, L121

Asano, K., & Nagataki, S. 2006, ApJ, 640, L9

Asano, K., & Terasawa, S. 2009, ApJ, 705, 1714

Band, D. et al. 1993, ApJ, 413, 281

Baring, M. G., 2006, ApJ, 650, 1004

Belmont, R., Malzac, J., & Marcowith, A. 2008, A&A, 491, 617

Beloborodov, A. M., 2005, ApJ, 618, L13

Beloborodov, A. M. 2010, MNRAS, 407, 1033

Berestetskii, V. B., Lifshitz, E. M., & Pitaevskii, L. P. 1982, Quantum Electrodynamics (New York: Pergamon), 371

Böttcher, M., & Dermer, C. D. 1998, ApJ, 499, L131

Bošnjak, Ž, Daigne, F., & Dubus, G. 2009, A&A, 498, 677

Brunetti, G., 2000, Astropart. Phys., 13, 107

Chen, L. et al., 2005, ApJ, 619, 983

Corsi, A. Guetta, D., & Piro, L. 2010, A&A, 524, 92

Daigne, F., Bošnjak, Ž., & Dubus, G. 2011, A&A, 526, 110

Daigne, F., & Mochkovitch, R. 1998, MNRAS, 296, 275

Daigne, F., & Mochkovitch, R. 2003, MNRAS, 342, 587

Derishev, E. V., Kocharovsky, V. V., & Kocharovsky, V., VI. 2001, A&A, 372, 1071

Fan, Y.-Z., Piran, T., Narayan, R., & Wei, D.-M. 2008, MNRAS, 384, 1483

Fenimore, E. E., Madras, C. M., & Nayakshin, S. 1996, ApJ, 473, 998

Ghisellini, G., Guilbert, P. & Svensson, R. 1988, ApJ, 334, L5

Ghisellini, G., Haardt, F., & Svensson, R. 1998, MNRAS, 297, 348

Ghisellini, G., & Svensson, R. 1991, MNRAS, 252, 313

Ghisellini, G. at al. 2010, MNRAS, 403, 926

Giannious, D., & Spruit, H. C. 2007, A&A, 469, 1

González, M. M., Dingus, B. L., Kaneko, Y., Preece, R. D., Dermer, C. D., & Briggs, M. S.
    2003, Nature, 424, 749

Granot, J., Cohen-Tanugi, J. & do Couto e Silva, E. 2008, ApJ, 677, 92

Guetta, D., & Granot, J. 2003, ApJ, 585, 885

Guetta, D., Spada, M., & Waxman, E. 2001b, ApJ, 559, 101

Gupta, N., & Zhang, B., 2007, MNRAS, 380, 78

Hakkila, J., & Giblin, T. W. 2004, ApJ, 610, 361

Hakkila, J. et al., 2008, ApJ, 677, L81

He, H.-N., Wu, X.-F., Toma, K., Wang, X.-Y., & Mészáros, P. 2011, ApJ, 733, 22

Inoue, T., Asano, K., & Ioka, K. 2011, ApJ, 734, 77

Ioka, K. 2010, Prog. Theor. Phys., 124, 667

Ioka, K., Murase, K., Toma, K., Nagataki, S., & Nakamura, T. 2007, ApJ, 670, L77

Ioka, K., & Nakamura, T. 2001, ApJ, 554, L163

Ioka, K., Ohira, Y., Kawanaka, N., & Mizuta, A. 2011, arXiv:1103.5746

Kneiske, T.M. et al. 2004, A&A, 413, 807

Kobayashi, S., Piran, T., & Sari, R. 1997, ApJ, 490, 92

Kocevski, D., & Liang, E. 2003, ApJ, 594, 385

Kumar, P., & Barniol Duran, R. 2010, MNRAS, 409, 226

Li, Z., 2010, ApJ, 709, 525

Lu, R.-J., Qin, Y.-P., Zhang, Z.-B., & Yi, T.-F. 2006, MNRAS, 367, 275

Maxham, A., Zhang, B. B., & Zhang, B. 2011, MNRAS, 415, 77

Mészáros, P. 2006, Rep. Prog. Phys., 69, 2259

Mészáros, P., & Rees, M. J. 1994, MNRAS, 269, L41

Mészáros, P., & Rees, M. J. 2000, ApJ, 530, 292

Mészáros, P., & Rees, M. J. 2011, ApJ, 733, L40

Mizuno, Y., at al. 2011, ApJ, 726, 62

Murase, K., Asano, K., & Nagataki, S. 2007, ApJ, 671, 1886

Murase, K., & Nagataki, S. 2006, Phys. Rev. D, 73, 3002

Murase, K., Toma, K., Yamazaki, R., & Mészáros, P. 2011, ApJ, 732, 77

Nakar, E., Ando, S., & Sari, R. 2009, ApJ, 703, 675

Norris, J. P. et al., 1996, ApJ, 459, 393

Paczýnski, B. 1986, ApJ, 308, L43

Panaitescu, A., & Mészáros, P. 2000, ApJ, 544, L17

Pe'er, A. 2008, ApJ, 682, 463

Pe'er, A., & Waxman, E. 2005, ApJ, 628, 857

Pe'er, A., & Zhang, B. 2006, ApJ, 653, 454

Pilla, R. P., & Loeb, A. 1998, ApJ, 494, L167

Piran, T. 2005, Rev. Mod. Phys., 76, 1143

Preece, R. D., Briggs, M. S., Mallozzi, R. S., Pendleton, G. N., Paciesas, W. S., & Band, D. L. 2000, ApJS, 126, 19

Racusin, J. L. et al., 2008, Nature, 455, 183

Rando, R. et al., 2009, arXiv:0907.0626

Rybicki, G. B., & Lightman, A. P. 1979, Radiative Processes in Astrophysics (New York: Wiley-Interscience)

Ryde, F., et al. 2010, ApJ, 709, L172

Shen, R.-F., Song, L.-M., & Li, Z. 2005, MNRAS, 362, 59

Toma, K., Wu, X.-F. & Mészáros, P. 2009, ApJ, 707, 1404

Toma, K., Wu, X.-F. & Mészáros, P. 2010, MNRAS, 415, 1663

Vietri, M. 1995, ApJ, 453, 883

Vurm, I., Beloborodov, A. M., & Poutanen, J. 2011, accepted for ApJ, arXiv:1104.0394

Vurm, I., & Poutanen, J. 2009, ApJ, 698, 293

Wang, X.-Y., Li, Z., Dai, Z.-G., & Mészáros, P. 2009, ApJ, 698, 98

Wang, X.-Y., & Mészáros, P. 2006, ApJ, 643, L95

Waxman, E. 1995, Phys. Rev. Lett., 75, 386

Waxman, E., & Bahcall, J. 1997, Phys. Rev. Lett., 78, 2292

Wu, B., & Fenimore, E. E. 2000, ApJ, 535, L29

Yonetoku, D., Murakami, T., Nakamura, T., Yamazaki, R., Inoue, A. K., & Ioka, K. 2004, ApJ, 609, 935

Zhang, B.-B., et al. 2011, ApJ, 730, 141

Zhang, F.-W., Qin, Y.-P., & Zhang, B.-B. 2007, PASJ, 59, 857

Zhang, W., MacFadyen, A., & Wang, P. 2009, ApJ, 692, 240

Zhao, X.-H., Li, Z., & Bai, J.-M. 2011, ApJ, 726, 89

Zou, Y.-C., Fan, Y.-Z., & Piran, T. 2011, ApJ, 726, 2